

The Role of Turbulence in an Intense Tropical Cyclone: Momentum Diffusion, Eddy Viscosities, and Mixing Lengths[©]

CHIBUEZE N. OGUEJIOFOR^①,^a GEORGE H. BRYAN,^b RICHARD ROTUNNO,^b PETER P. SULLIVAN,^b AND DAVID H. RICHTER^a

^a University of Notre Dame, South Bend, Indiana

^b NSF National Center for Atmospheric Research, Boulder, Colorado

(Manuscript received 2 November 2023, in final form 4 May 2024, accepted 3 June 2024)

ABSTRACT: Improved representation of turbulent processes in numerical models of tropical cyclones (TCs) is expected to improve intensity forecasts. To this end, the authors use a large-eddy simulation (with 31-m horizontal grid spacing) of an idealized category 5 TC to understand the role of turbulent processes in the inner core of TCs and their role on the mean intensity. Azimuthally and temporally averaged budgets of the momentum fields show that TC turbulence acts to weaken the maximum tangential velocity, diminish the strength of radial inflow into the eye, and suppress the magnitude of the mean eyewall updraft. Turbulent flux divergences in both the vertical and radial directions are shown to influence the TC mean wind field, with the vertical being dominant in most of the inflowing boundary layer and the eyewall (analogous to traditional atmospheric boundary layer flows), while the radial becomes important only in the eyewall. The validity of the downgradient eddy viscosity hypothesis is largely confirmed for mean velocity fields, except in narrow regions which generally correspond to weak gradients of the mean fields, as well as a narrow region in the eye. This study also provides guidance for values of effective eddy viscosities and vertical mixing length in the most turbulent regions of intense TCs, which have rarely been measured observationally. A generalized formulation of effective eddy viscosity (including the Reynolds normal stresses) is presented.

SIGNIFICANCE STATEMENT: This study uses a turbulence-resolving simulation of a category 5 tropical cyclone to understand the role of turbulence in intense storms. Results show that turbulence clearly modulates storm structure and intensity. This study provides guidance for the values of turbulent quantities (which are usually parameterized in comparatively coarse operational TC forecast models) in scarcely observed regions of intense storms. Furthermore, a complete formulation of the effective eddy viscosities is proposed, incorporating contributions from typically ignored Reynolds normal stress terms.

KEYWORDS: Atmosphere; Boundary layer; Tropical cyclones; Large-eddy simulations; Subgrid-scale processes

1. Introduction

Accurate prediction of hurricane intensity continues to lag behind track prediction (Rogers et al. 2006; DeMaria et al. 2014; Cangialosi et al. 2020), partly due to the lack of sufficiently high-resolution spatiotemporal observations of small-scale processes within the hurricane boundary layer (HBL) (Zhang et al. 2009; Emanuel 2017), defined roughly as the first kilometer above the surface in TCs. Incomplete representation of turbulence and its various parameterized roles in numerical weather models may be a substantial source of hurricane-intensity forecast error, especially in the short time range (e.g., rapid intensification events). This is partly because turbulent fluxes in the hurricane boundary layer, which are mostly parameterized using schemes developed for nonhurricane wind conditions (Chen et al. 2021; Chen 2022), modulate enthalpy, moisture, and momentum exchange between the storm and the underlying ocean surface. Flight-level and ground-based

observations of the near-eyewall region in intense hurricanes have alluded to the existence of organized turbulent structures in the hurricane boundary layer (Montgomery et al. 2006; Marks et al. 2008; Aberson et al. 2017). These structures, sometimes identified as coherent eddies (Guimond et al. 2018; Protzko et al. 2023), tornado-scale vortices (Wurman and Kosiba 2018), mesovortices (Kossin and Schubert 2004; Alford et al. 2023), or boundary layer roll vortices (Wurman and Winslow 1998; Morrison et al. 2005; Lorsolo et al. 2008; Foster 2005, 2013) based on their sizes, orientation, intensity, and proximity to the eyewall (Li and Pu 2023), can have important implications ranging from modulating the severity of damage caused by hurricanes during landfall (Wurman and Kosiba 2018; Rozoff et al. 2023) to endangering research flight missions (Marks et al. 2008; Zhang et al. 2010). In addition, these structures could have significant influence on the magnitude of the fluxes in the HBL (Morrison et al. 2005), thereby affecting the overall storm dynamics. Very few crewed aircraft missions have been able to observe these structures, especially within the intense turbulence regime of the hurricane inner eyewall. One such mission flown by the National Oceanic and Atmospheric Administration (NOAA) WP-3D research aircraft encountered a series of intense updrafts and downdrafts while penetrating the eyewall of Hurricane Hugo (1989)—a category 5 storm—causing the loss of one of its four engines (Masters 1999; Marks et al. 2008).

[©] Supplemental information related to this paper is available at the Journals Online website: <https://doi.org/10.1175/JAS-D-23-0209.s1>.

Corresponding author: Chibueze N. Oguejiofor, coguejio@nd.edu

Since then, small uncrewed aircraft system (sUAS) (Cione et al. 2016, 2020; Aksoy et al. 2022; Darko et al. 2022; Sellwood et al. 2023) and mobile Doppler radars (Wurman and Winslow 1998; Kosiba and Wurman 2014; Wurman and Kosiba 2018) have been deployed within the inner eyewall region of intense hurricanes, in an attempt to safely understand the role of these structures in modulating the storm dynamics and the HBL in general.

The HBL has been previously shown to play an important role in mixing and energy transport which modulates the intensity of hurricanes (Emanuel 1997; Bryan and Rotunno 2009; Smith and Montgomery 2010; Bryan 2012). Using a series of numerical simulations, Bryan (2012); Rotunno and Bryan (2012) concluded that the parameterization of turbulence (in the horizontal direction) in the HBL substantially affects the maximum intensity of simulated storms. Rogers et al. (2012) showed that the turbulence kinetic energy (TKE) is maximized in the hurricane eyewall and “corner” region (where the mean flow changes from primarily horizontal toward the TC center, to primarily upward in the eyewall). These studies provide quantitative evidence for the inhomogeneous nature of hurricane turbulence. Furthermore, studies have shown a height-dependent (Byrne and Zhang 2013) and radius-dependent (Tang et al. 2015) transition from 3D to 2D turbulence in TCs, suggesting an inverse (upscale) energy cascade above ≈ 150 m in the TC boundary layer as well as in the inner-core region (i.e., $< 1.5 \times$ the radius of maximum winds). Since organized turbulent structures are prevalent in the HBL, it is necessary to understand their characteristic scales and roles in flux/energy flow (into and away from the HBL) in order to understand the dynamics of intensity changes in hurricanes.

Although many important aspects of hurricane structure and behavior have been discovered using aircraft observations (Aberson et al. 2006a), the general distribution of turbulence in hurricanes has only recently been analyzed. Lorsolo et al. (2010) used airborne Doppler radar to provide, for the first time, the radial-height distribution of TKE in a number of hurricanes. In situ turbulence measurements (Zhang et al. 2010; Zhang and Montgomery 2012) have been used to estimate the eddy diffusivity in the hurricane boundary layer and eyewall. Although these particular measurements are more localized within the hurricane, they suggest that hurricane turbulence may be strongly anisotropic in that the horizontal diffusivity in the eyewall was found to be approximately an order of magnitude greater than the vertical diffusivity in the boundary layer. Using the Imaging Wind and Rain Airborne Profiler (IWRAP) with a horizontal and vertical resolution of 250 and 30 m, respectively, Guimond et al. (2018) documented that the most intense coherent eddy activities were preferentially located in the inner edge of the eyewall after the concentric eyewall replacement cycle stage of Hurricane Rita (2005), with typical radial wavelengths of $\sim 1\text{--}3$ km and a depth of ~ 1.5 km.

Numerical models have also been used extensively to study the evolution of the HBL and intensity changes in hurricanes. However, they are sensitive to the parameterization of turbulence, particularly that of horizontal turbulent diffusion

(Bryan and Rotunno 2009; Rotunno and Bryan 2012). Rotunno et al. (2009) pointed out the absence of any observational, experimental, or theoretical basis for existing parameterizations of horizontal diffusion and promoted using the technique of large-eddy simulation (LES) for an idealized hurricane to obtain a physically based representation. In the years since that paper was published, there have been major advances in computer power and the use of LES for atmospheric applications (Moeng and Sullivan 2014). With LES, the large energy-containing turbulent eddies responsible for most of the energy production are explicitly resolved [as opposed to the planetary boundary layer (PBL) parameterization schemes used by traditional numerical weather prediction (NWP) models], while only small and much-less-energetic eddies are parameterized.

Using a horizontal grid interval of 100 m in the innermost domain of the Weather Research and Forecasting LES (WRF-LES), Zhu (2008) analyzed the existence of the so-called coherent large-eddy circulations (LECs) and concluded that they exist as well-defined updraft–downdraft couplets that enhance the exchange of energy, moisture, and momentum. Ito et al. (2017) identified the existence of small-scale coherent structures and three types of roll structures (depending on proximity to the hurricane eye), using the Japan Meteorological Agency nonhydrostatic model (JMA-NHM) run at a horizontal grid interval of 100 m. Wu et al. (2018) and Wu et al. (2019) identified tornado-scale vortices (TSVs) in their 37-m WRF-LESs having a horizontal scale of ≈ 1 km with associated updrafts of $> 15 \text{ m s}^{-1}$, occurring preferentially in the inner edge of the eyewall; they noted that each TSV comprised of a couplet of narrow intense updraft and a broad downdraft. Using a WRF-LES with a 31-m grid interval, Cécé et al. (2021) simulated the evolution of Hurricane Irma (a category 5 storm), showing that extreme wind gusts ($\approx 132 \text{ m s}^{-1}$) were associated with multiple subtornadic-scale vortices. Liu et al. (2022) examined the relationship between TSVs and enhanced surface wind gusts using a one-way nested WRF-LES (with a horizontal grid interval of 37 m in the innermost domain). Most recently, Li and Pu (2023) characterized roll vortices and associated turbulent eddies aloft within 20–40-km radii of a simulated landfall of Hurricane Harvey (using data from a WRF-LES with a 100-m grid interval), reporting a mean wavelength of 0.9–1.1 km for turbulent eddies and 0.8 km for roll vortices.

Clearly, understanding the prevalence and role of these coherent turbulent structures in the hurricane eyewall is pertinent not only to research flight safety but also to the understanding of heat, momentum, and moisture flux which determines the bounds of storm intensity predictability (Emanuel 1986; Holland 1997). Most importantly, regarding HBL parameterizations, understanding the complex interaction among turbulent eddies of varying scales is a critical task in order to account for the net vertical fluxes which affect the storm. In the present study, LES of the inner core (i.e., eye, eyewall, and nearby rainbands) is utilized to characterize the behavior of coherent turbulent eddies responsible for vertical and horizontal fluxes within a simulated category 5 hurricane and their role in

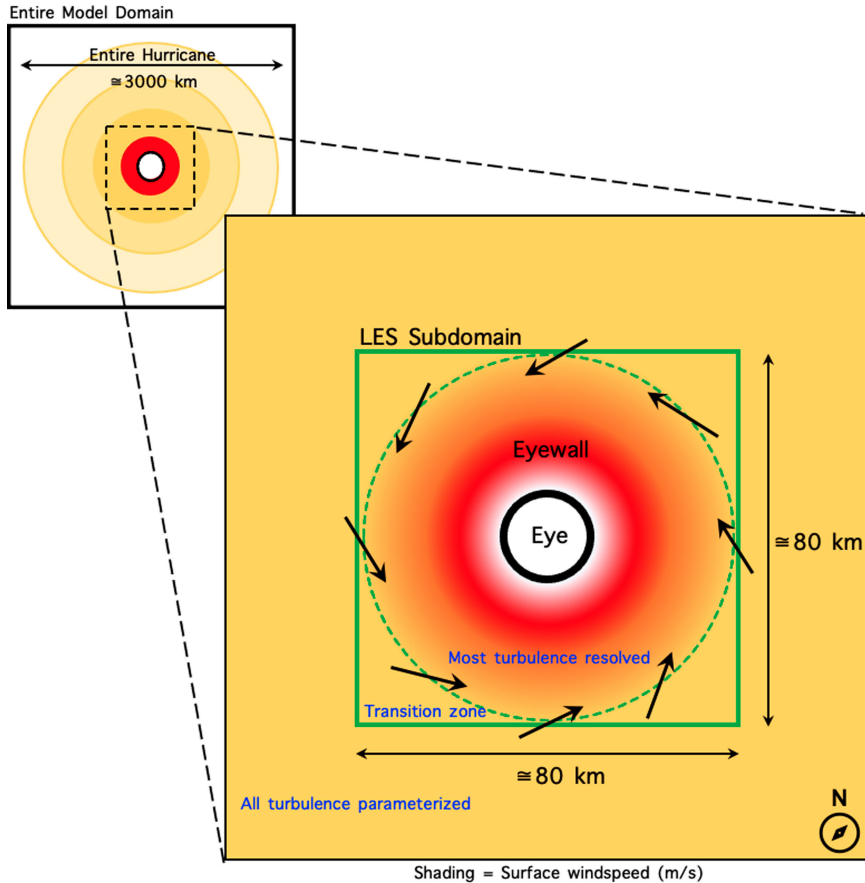


FIG. 1. Schematic showing the model-simulation setup. The green box (LES subdomain) represents the region on which the analysis presented in this study is focused. Color shading qualitatively represents near-surface wind speed, with red colors being the highest values.

the budget of the mean wind field. Specific objectives of this study include the following:

- 1) Understanding the effects of turbulence on the mean wind field of an intense tropical cyclone.
- 2) Examining the validity of the widely used downgradient eddy viscosity hypothesis.
- 3) Analyzing the vertical and horizontal turbulence momentum fluxes in the TC boundary layer, with implications on effective eddy viscosity and mixing length, specifically in the highly turbulent eyewall region of the storm.

The remainder of this paper is organized as follows. Section 2 describes the LES modeling framework used in this study to investigate the existence of turbulence and coherent eddies in the HBL. Section 3 reports the major results of this study and these results are further discussed and summarized with concluding remarks in section 4.

2. Simulation methodology

This study uses the same simulation as in Worsnop et al. (2017), Stern and Bryan (2018), Stern et al. (2021), and Richter et al. (2021). Specifically, Cloud Model 1 (CM1) (Bryan and

Fritsch 2002; Bryan and Rotunno 2009) was used to simulate an idealized category 5 hurricane at turbulence-resolving horizontal and vertical grid intervals ($\Delta x = \Delta y = 31.25$ m, $\Delta z = 15.625$ m), utilizing the modeling framework described in Bryan et al. (2017a). The simulation, although idealized, was inspired by Hurricane Felix (2007), which was a category 5 storm with a comparatively small radius of maximum reflectivity of about 11 km (Aberson et al. 2017).

Figure 1 summarizes the idealized hurricane LES setup, as also described in Bryan et al. (2017a) for tornadoes. The three-dimensional model is initialized with output from an axisymmetric CM1 simulation, which in this case was run for 12 days until a quasi-steady state is reached. Time-averaged variables were then used to initialize the LES run. The initially axisymmetric eyewall convection quickly (within about 10 min) transforms into three-dimensional motion. The simulated storm takes roughly 1 h to adjust from the axisymmetric initial state with parameterized turbulence to a 3D flow with resolved turbulence; our analysis excludes this period of adjustment.

The 3D LES was run for a total of 6 h, reaching a statistically steady state (defined below) after about 1 h of model integration. By design, the present idealized hurricane is statistically homogeneous in the azimuthal direction as the vortex is

not translating relative to the lower boundary nor is the beta-effect or vertical wind shear included. The entire model domain spans $3000 \text{ km} \times 3000 \text{ km} \times 25 \text{ km}$, which is large enough to contain the full hurricane and its environment including the inner core and nearby rainbands. However, the LES subdomain is a smaller subset ($80 \text{ km} \times 80 \text{ km} \times 3 \text{ km}$), which is large enough to produce turbulence from the eye to about 3 times the radius of maximum winds. Within the inner LES subdomain, a constant grid interval of 31.25 and 15.625 m is used in the horizontal and vertical, respectively. For the subgrid turbulence within the fine-mesh domain, a two-part subgrid-scale TKE model based on the Deardorff TKE scheme is used (Deardorff 1980; Bryan et al. 2017b). Outside of the fine-mesh LES domain, where turbulence is parameterized using the Louis PBL scheme (Louis 1979; Kepert 2012), the stretched horizontal grid reaches 15-km grid spacing at the edge of the domain, while the vertical grid spacing stretches to 500 m at 8-km height, staying constant at 500 m up to the top of the model domain.

One of the challenges for LES in a domain where the flow enters without turbulence from a coarser-grid domain (e.g., Muñoz-Esparza et al. 2014; Munters et al. 2016; Sullivan et al. 2020) is for the model to develop realistic, resolved turbulence quickly given an air parcel's short transit time through the fine-grid domain (green box in Fig. 1). To make sure the boundary layer turbulence becomes fully developed as the boundary layer flow transitions from the coarse grid to the fine, a separate precursor LES of the hurricane boundary layer for the flow beyond the LES subdomain is used to initiate turbulence in a transition zone (Fig. 1) [see details in Bryan et al. (2017a)].

For cloud microphysics, the double-moment scheme of Morrison et al. (2009) is used in the entire simulation domain. The parameterization of surface stress is described in Bryan et al. (2017b); most of the LES subdomain has average 10-m wind speed above 25 m s^{-1} , for which the surface roughness length z_0 is constant at 2.8 mm. Surface heat fluxes assume a constant exchange coefficient of 1.2×10^{-3} . No radiation scheme is used, although the simple relaxation method of Rotunno and Emanuel (1987) (hereafter RE87) is used for temperature; this tendency is negligibly small in the LES subdomain. Further details of the modeling setup, as well as additional analyses of this simulation, are available in Stern and Bryan (2018).

When analyzing turbulent flows, it can be challenging to obtain robust results that reveal insights into the role of the turbulent eddies in a seemingly chaotic flow (e.g., Moeng and Sullivan 2014). Typically, a combination of space- and time-averaging is used to define mean fields, with perturbations from those means being used to define turbulent fluxes and variances. Large datasets are often required to obtain reliable results. To this end, for analyses presented in the following section, the model was “restarted” after 4 h and integrated for an additional 1 h with output every 30 s. Hence, there are 121 snapshots of simulation output from $t = 14\,400 \text{ s}$ to $t = 18\,000 \text{ s}$ for the following analyses. The analysis procedure is nearly the same as in section 4 of Nolan et al. (2017). First, all variables are time averaged at relevant points on the model's C-staggered Cartesian grid. At this stage, the exact same numerical methods that were used in the model integration (e.g., Wicker and

Skamarock 2002) are used in the analysis, e.g., for interpolation on the staggered grid; we find this approach to be necessary to yield small residuals in budgets of mean model variables (e.g., winds, temperature, and moisture). Then, perturbations from this time-averaged state are calculated at all time levels and are used to calculate second-order statistics such as vertical flux of momentum (e.g., $u'w'$); these results are then time averaged to obtain average turbulence fluxes and variances at each grid point. Last, all variables are azimuthally averaged and presented in radius–height (r, z) coordinates; this last step is effective as a “smoother” of the results because there are many (i.e., thousands) of time-averaged profiles in original model coordinates with this resolution. The resulting mean field from this procedure for quantity $\chi(x, y, z, t)$ is denoted by $\langle \chi \rangle(r, z)$ and perturbations by $\chi' = \chi - \langle \chi \rangle$.

Resulting mean-field budgets, described in the next section and the appendix, have very small residuals; the sum of all terms on the rhs of the mean-velocity budget equations peaks at 0.02 m s^{-2} (not shown). In comparison, the inertial terms in the budget exceed 0.2 m s^{-2} , and the lhs of these budgets (the change of $\langle \chi \rangle$ over the analysis time) is on the order of 0.001 m s^{-2} (hence, the flow is not strictly steady but can be considered practically steady state). The smallness of the budget residual and the time-tendency terms provide confidence in the methodology described in the previous paragraph.

3. Results

Figure 2 shows sample horizontal slices at $z \approx 40, 100, 700$, and 1500 m of the vertical velocity field w (m s^{-1}) in the southwest quadrant of the storm center, where the solid vertical line roughly cuts through the center ($r \approx 0 \text{ km}$) of each slice. From Fig. 2, it is clear that vertical velocity fluctuations close to the surface ($z \approx 40$ and 100 m) are weaker than at the upper levels ($z \approx 700$ and 1500 m), indicating the influence of the surface boundary (Panofsky 1953; Panofsky and McCormick 1960). The horizontal scale of turbulent velocity structures is seen to increase with distance from the surface. In addition, at $z \approx 700$ and 1500 m , the eyewall of the TC is clearly defined by the predominantly positive vertical velocity values around the eye, indicative of strong updrafts. Furthermore, above the lower levels, “streaks” (defined here as a linear organization) in the patterns of w are seen outside the eyewall region. The vertical velocity field is clearly turbulent, with different scales of spatial coherence ranging from well-organized elongated streaks to seemingly unorganized patches of updrafts and downdrafts.

Focusing on $z \approx 700 \text{ m}$, Figs. 3a and 3b show a windowed-in sample of the vertical velocity and water vapor mixing ratio fields for just the southwest quadrant of the storm (same as in Fig. 2). In Fig. 3a, there are a number of kilometer-scale intense updraft-downdraft couplets in the inner edge of the eyewall (two of which are highlighted by the arrows), with changes in the magnitude of $w \geq 10 \text{ m s}^{-1}$ across the couplets, in some cases. The magnitudes of these updraft-downdraft pairs seen here are also similar to those seen in field observations of intense storms (Stern et al. 2016). For example, in Hurricane Felix (a category 5 storm in 2007), the NOAA42 research aircraft experienced a sequence of 10 m s^{-1}

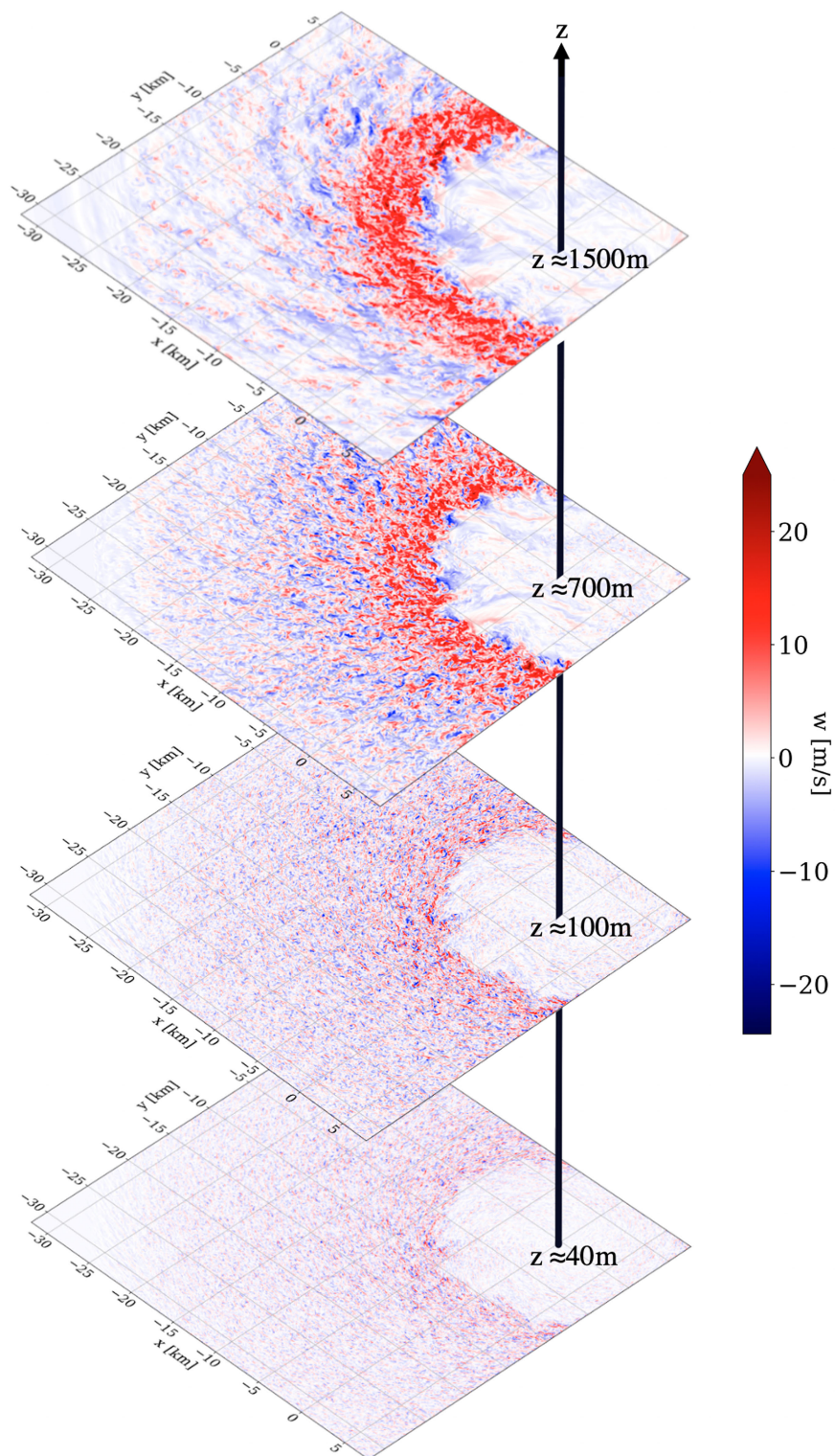


FIG. 2. Horizontal cross sections of the vertical velocity field w (m s^{-1}) around the southwest quadrant of the storm, at different heights. The black vertical arrow passes through the eye of the storm.

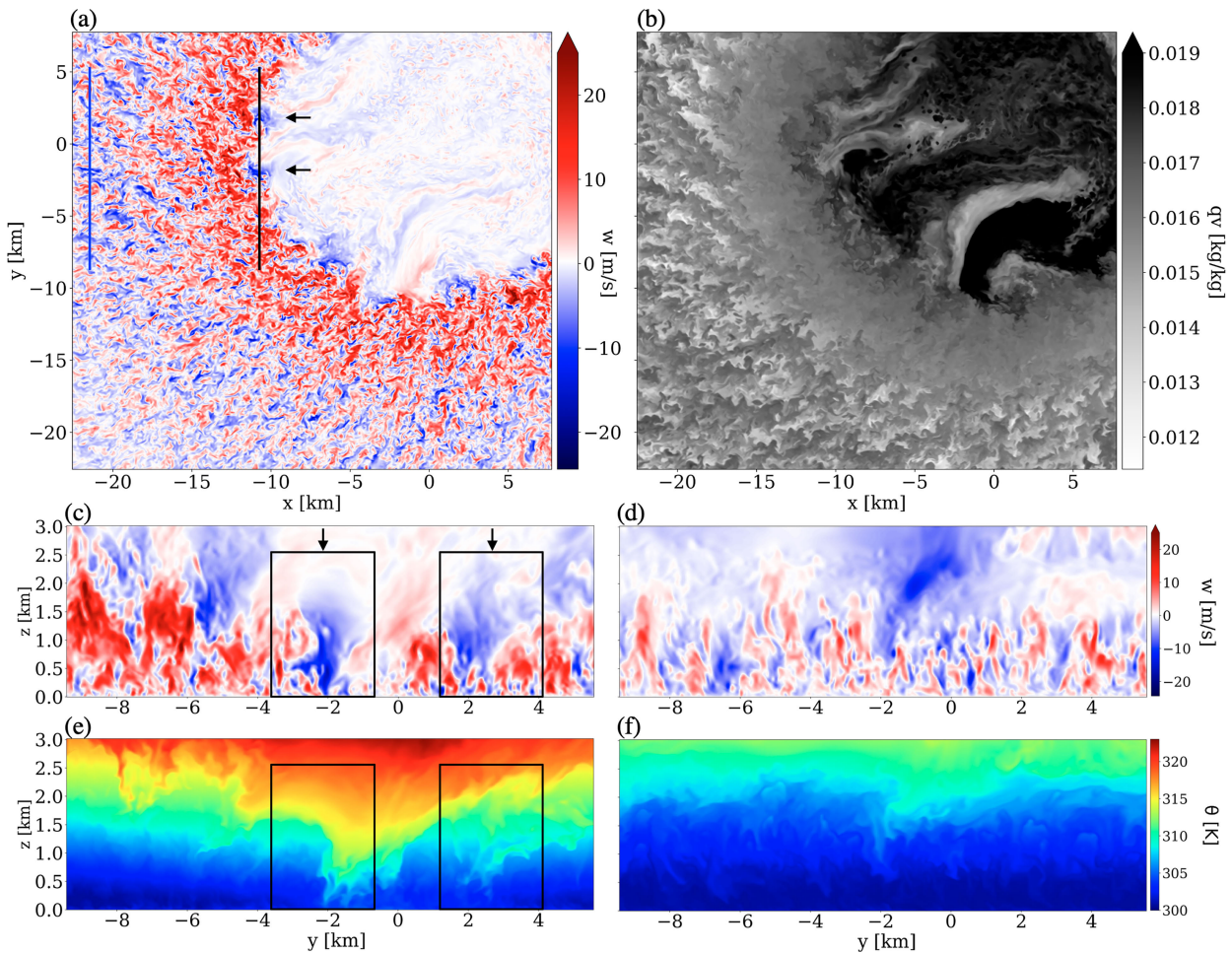


FIG. 3. Windowed-in horizontal cross sections of (a) vertical velocity (m s^{-1}) in the southwest quadrant of the LES model domain and (b) water vapor mixing ratio (kg kg^{-1}), at $z \approx 700$ m. Vertical cross sections of (c) vertical velocity (m s^{-1}) and (e) potential temperature (K) in the inner eyewall ($r \approx 11$ km). Vertical cross sections of (d) vertical velocity (m s^{-1}) and (f) potential temperature (K) outside the eyewall ($r \approx 22$ km). The black and blue lines in (a) represent the locations (inner eyewall and outside the eyewall, respectively) from which the vertical sections in (c) and (e) and (d) and (f) are plotted, respectively. The boxes in (c) and (e) highlight the vertical extent of two kilometer-scale intense downdraft features in (a).

downdraft, 31 m s^{-1} updraft, and 7 m s^{-1} downdraft within 1 min (Aberson et al. 2017). These features, distributed along the inner edge of the eyewall, are also quite similar to those documented in several observations of intense storms (Aberson et al. 2006b; Tsukada and Horinouchi 2020). The sizes of these coherent velocity structures appear to decrease with increasing radial distance from the storm center. In addition, visibly elongated streaks of negative velocity signatures are seen farther from the eye, roughly inclined toward the eye of the storm. The shape of these quasi-linear streaks quickly deform from their elongated form farther from the eye, to a more compact cellular form in the inner edge of the eyewall region. In the simulated mixing ratio q_v plot shown in Fig. 3b, the structure in the southern part of the inner eyewall, i.e., ranging from $x \approx -5$ to 5 km at $y \approx -12$ km, is qualitatively similar to the mesovortices (MVs) identified in the inner eyewall of Hurricane Harvey (a category 4 storm in 2007) by Wurman and Kosiba (2018) and Alford et al. (2023) using

Doppler radar, as is the associated collocated vertical velocity signature in Fig. 3a. The MVs documented by Alford et al. (2023) were found to be associated with intense updrafts (quite similar to our study), around wind field perturbations of about $5\text{--}10 \text{ m s}^{-1}$. In a quantitative study of eyewall MVs (using the *Himawari-8* satellite imagery) and their role in the enhancement of inner-core rotation by angular momentum transport, Tsukada and Horinouchi (2020) also identified features rotating in the inner eyewall of Typhoon Lan (2017) which are strikingly similar to Fig. 3b. Similar features (i.e., large-scale MVs of $\approx 20\text{--}30$ km in size) were also documented in Hurricane Karl (2010) by Guimond et al. (2016), adjacent to convective bursts, and were shown to be transporting air across the eye–eyewall interface. These types of features are clearly present in this simulation.

A vertical cross section through these structures in the vertical velocity field at $r \approx 11$ km (inner eyewall, black line) and $r \approx 22$ km (outside the eyewall, blue line) is shown in Figs. 3c

and 3d, respectively. Two intense downdrafts (highlighted by the arrows in Fig. 3a) are identified in Fig. 3c, showing a vertical extent of ≈ 2.5 km and associated vertical transport indicated by the signatures from the cross section of potential temperature at the same location and time (Fig. 3e). Farther from the inner eyewall (blue line at $r \approx 22$ km in Fig. 3a), a vertical cross section of the same variables (Figs. 3d,f) shows a smaller and weaker updraft-downdraft couplet.

From Figs. 2 and 3, it is clear that this simulation produces several mesovortex-type structures and coherent turbulent eddies whose magnitude, spatial distribution, and associated updraft-downdraft couplets are consistent with observational studies (see animations of Figs. 3a,b in the online supplemental material). These figures and animations also reveal a potential disadvantage of our analysis methodology (section 2), in that all of these coherent structures are included in our analysis, even though some kilometer-scale features may not be considered “turbulence” by traditional textbook definitions. Indeed, some of these features could be resolvable using even 1-km horizontal grid spacing and would not need to be included in a turbulence (i.e., PBL) parameterization. Nevertheless, we see no easy way to remove the kilometer-scale features from our analysis, and the resulting analyses are insightful, even if the direct application to operational PBL parameterization is uncertain. The rest of this paper is focused on understanding the roles of these turbulent eddies in modulating the mean flow around the TC eyewall region.

a. The mean velocity fields

Before addressing the role of turbulence on the mean field, it is important to have a clear picture of the mean flow field itself. The geometry of a mature TC makes the cylindrical coordinate system particularly useful in representing its dynamics. Here, we discuss the magnitude and direction of the azimuthally and time-averaged velocity components in Fig. 4. Figures 4a–c show the radius–height plots of the azimuthally and time-averaged velocity components, showing the expected radial variation of velocity fields seen in observations (e.g., Rogers et al. 2012; Zhang et al. 2023). Figure 4a shows that the maximum tangential velocity is at a radius of $r \approx 11$ km near the surface and slopes outwards with height. Mean tangential velocity decreases steadily with increasing radii beyond the eyewall, while also decreasing to zero toward the eye ($r \approx 0$ km). Figure 4b shows that the radial velocity is negative close to the surface, indicating strong inflow toward the eyewall region, which decreases with height until it becomes positive aloft, typical of the HBL. The level of maximum inflow is 50–75 m, slightly lower but consistent with observations (Zhang et al. 2011; Ming et al. 2015; Ahern et al. 2019; Zhang et al. 2023). Figure 4c shows that the mean vertical velocity is weak in most of the HBL except in the eyewall ($r \approx 10$ –17 km—highlighted by the black solid contour), where it is clearly positive, indicating a strong mean updraft characteristic of intense eyewall convection. A notable mean downdraft (indicated by negative vertical velocity, blue shading) is seen just outside of the eyewall ($r \approx 21$ km).

Together, the azimuthally and time-averaged velocity field plots shown in Figs. 4a–c (summarized in Fig. 4d) indicate maximum radial inflow and weak vertical velocity at the outer edge of the eyewall ($r \approx 17$ km) and close to the surface. As the mean radial inflow approaches the inner eyewall ($r \approx 11$ km), it reduces to zero in the corner-flow region, the region within the inner edge of the eyewall where the strong radial inflow slows down and turns upward through mass continuity; here, the vertical velocity substantially increases to a maximum above the BL (which we define roughly as the first 1 km above the surface). This flow pattern shows that the mean trajectory of air parcels follows an inflow path toward the core, followed by a deceleration and a sharply defined mean updraft in the eyewall region, consistent with previously well-established understanding of the mean structure of the TC boundary layer (Shea and Gray 1973; Marks and Houze 1987; Kepert and Wang 2001; Smith et al. 2009; Rogers et al. 2012; Persing et al. 2013; Montgomery and Smith 2014, 2017). We now move toward understanding the impact of turbulence on this mean flow.

b. Mean-field budget—The role of turbulent eddies

As shown above, coherent turbulent velocity structures are prevalent in the TC boundary layer, particularly in the eyewall. The question thus arises as to what role they play in the budget of the mean wind field equations. Do they act to enhance momentum in the eyewall or do they act to weaken it? To clarify the role of turbulent eddies, we derive the azimuthally and time-averaged momentum equations [in cylindrical coordinates, similar to Hinze (1959), Gray (1966), Stanisic (2012), Nolan et al. (2017)] and compute each term appearing on the right-hand side from the model simulation output:

$$\frac{\partial \langle u \rangle}{\partial t} = -\langle u \rangle \frac{\partial \langle u \rangle}{\partial r} - \langle w \rangle \frac{\partial \langle u \rangle}{\partial z} - \underbrace{\frac{1}{r} \frac{\partial}{\partial r} \langle ru'^2 \rangle}_{T_r^u} - \underbrace{\frac{\partial}{\partial z} \langle u'w' \rangle}_{T_z^u} + \frac{\langle v \rangle^2}{r} + \frac{\langle v'^2 \rangle}{r} - \frac{\partial \langle \phi \rangle}{\partial r} + f \langle v \rangle + \langle F^u \rangle, \quad (1)$$

$$\frac{\partial \langle v \rangle}{\partial t} = -\langle u \rangle \frac{\partial \langle v \rangle}{\partial r} - \langle w \rangle \frac{\partial \langle v \rangle}{\partial z} - \underbrace{\frac{1}{r^2} \frac{\partial}{\partial r} \langle r^2 u'v' \rangle}_{T_r^v} - \underbrace{\frac{\partial}{\partial z} \langle v'w' \rangle}_{T_z^v} - \frac{\langle u \rangle \langle v \rangle}{r} - f \langle u \rangle + \langle F^v \rangle, \quad (2)$$

$$\frac{\partial \langle w \rangle}{\partial t} = -\langle u \rangle \frac{\partial \langle w \rangle}{\partial r} - \langle w \rangle \frac{\partial \langle w \rangle}{\partial z} - \underbrace{\frac{1}{r} \frac{\partial}{\partial r} \langle ru'w' \rangle}_{T_r^w} - \underbrace{\frac{\partial}{\partial z} \langle w'^2 \rangle}_{T_z^w} - \frac{\partial \langle \phi \rangle}{\partial z} + F_b + \langle F^w \rangle. \quad (3)$$

Because this simulation is statistically steady, the lhs of the equations above is negligible (see section 2). The symbols u , v , and w represent the radial, tangential, and vertical velocity components; r is the radius; f is the Coriolis parameter; ϕ is

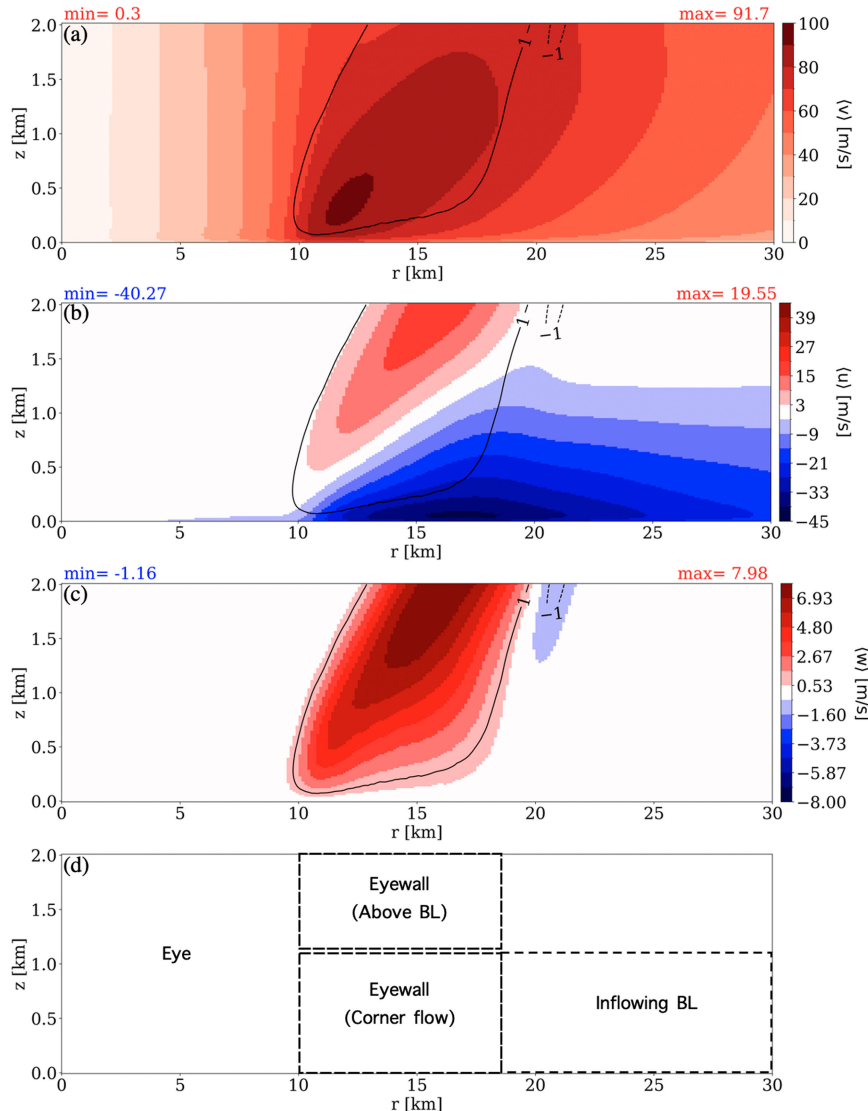


FIG. 4. Plots of the azimuthally and time-averaged velocity components for (a) tangential velocity $\langle v \rangle$ (m s^{-1}), (b) radial velocity $\langle u \rangle$ (m s^{-1}), and (c) vertical velocity $\langle w \rangle$ (m s^{-1}). The solid and dashed black contour lines in each panel indicate $\langle w \rangle$ at $\pm 1.0 \text{ m s}^{-1}$, highlighting the eyewall region and a significant downdraft feature just outside the eyewall, respectively. (d) Plot showing the nomenclature used in the identification of regions in the simulation; the top of the BL is considered to be roughly (but not strictly) at 1 km.

the density-normalized pressure; F_b is the buoyancy (see Bryan and Fritsch 2002); and the terms with a prime ('') indicate differences from the mean. The symbols F^u , F^v , and F^w represent contributions from the LES subgrid tendencies. In (1)–(3), the third and fourth terms ($T_r^{u/v/w}$ and $T_z^{u/v/w}$) on the rhs represent the momentum tendencies due to the divergence of the turbulent eddy fluxes in the radial and vertical directions, respectively. To understand the role of turbulence in the evolution of the mean wind field, we evaluate the contributions of these turbulent tendencies below. In all of the plots shown in Fig. 5, the subgrid contribution (in the radial $\langle F_r^{u/v/w} \rangle$ and vertical $\langle F_z^{u/v/w} \rangle$ directions)—which are negligible except

in the lowest few model levels—is included with the resolved terms. See the appendix for a comparative analysis of resolved and parameterized turbulent tendencies on the mean flow where the subgrid part is seen to be relevant only in the lowest model levels. In the appendix, we also briefly comment on the tendencies from the mean advection and other nonturbulence terms which appear in (1)–(3).

For the $\langle u \rangle$ budget in (1), Figs. 5a and 5b show the contribution to the mean flow by the turbulence flux divergences in the radial and vertical directions. The black contours indicate the mean radial velocity $\langle u \rangle$ (with a contour interval of 5 m s^{-1}). Both radial and vertical eddy tendencies act to

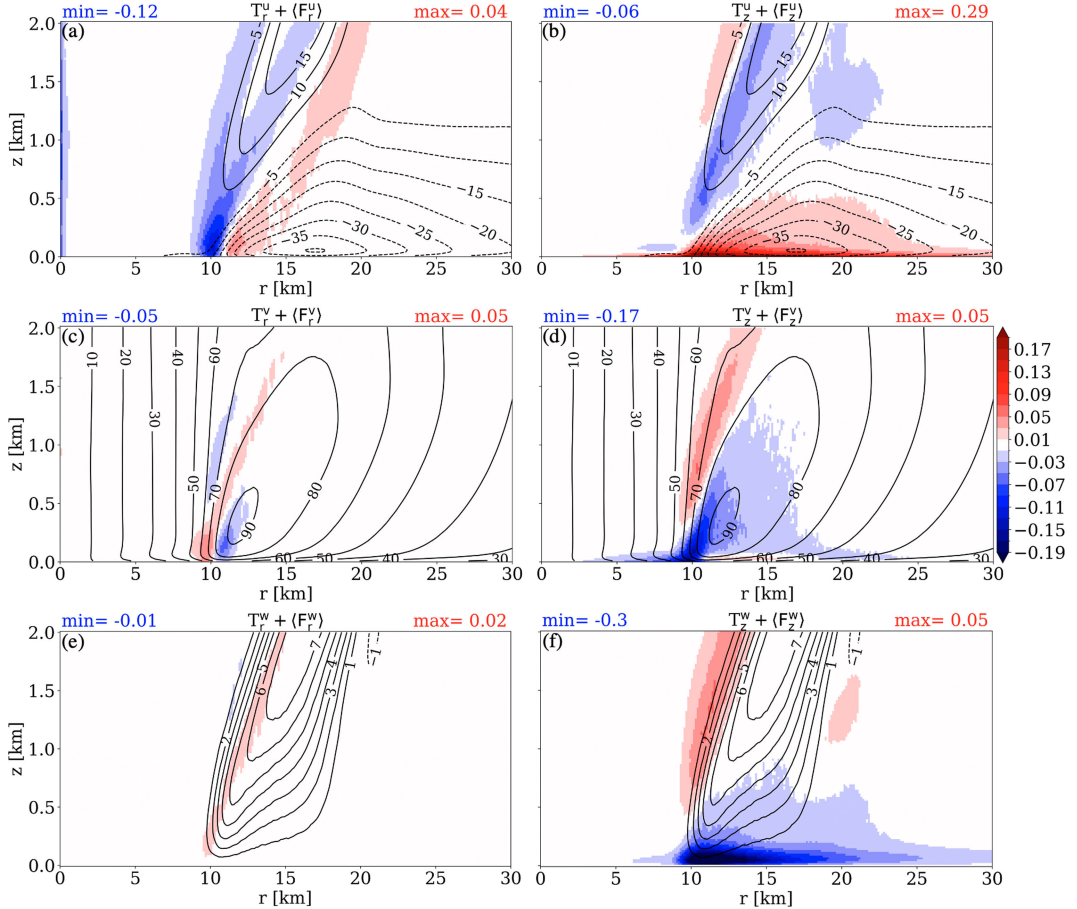


FIG. 5. Contour plots of azimuthally and time-averaged radial velocity field $\langle u \rangle$, overlaid with shadings from the contributions due to turbulent eddy tendencies in the (a) radial ($T_r^u + \langle F_r^u \rangle$) (m s^{-2}) and (b) vertical ($T_z^u + \langle F_z^u \rangle$) (m s^{-2}) directions. Analogous plots for the average tangential velocity field $\langle v \rangle$ for (c) $T_r^v + \langle F_r^v \rangle$) and (d) $T_z^v + \langle F_z^v \rangle$. Analogous plots for the average vertical velocity field $\langle w \rangle$ for (e) $T_r^w + \langle F_r^w \rangle$ and (f) $T_z^w + \langle F_z^w \rangle$.

weaken the magnitude of the radial velocity in the inflow region. From Fig. 5a, the radial tendency field is a dipole at $r \approx 11 \text{ km}$, indicating diffusion of radial inflow along the strong gradient of $\langle u \rangle$. Furthermore, the vertical eddy-flux divergence (Fig. 5b) primarily acts to diminish the magnitude of radial inflow close to the surface (from the inflow BL to the corner flow), ultimately leading to the loss of momentum due to drag. A comparison of the radial and vertical eddy tendencies here indicates that the weakening role (red shading) of the vertical term is significantly larger, especially closer to the surface (below the height of maximum radial inflow).

For the $\langle v \rangle$ budget, Figs. 5c and 5d show the contribution to the mean flow by the turbulence flux divergences in the radial and vertical directions. The black contours indicate the azimuthally and time-averaged tangential velocity $\langle v \rangle$ which peaks near the inner edge of the eyewall. Because of the negative values of eddy tendencies in the vicinity of V_{\max} , both the radial and vertical eddy tendencies act to weaken the maximum value of the tangential wind speed. In Fig. 5c, the radial eddy tendency is a dipole just inward of the eyewall ($r \approx 10 \text{ km}$) and thus acts to diffuse momentum at the eye-

eyewall interface. The vertical eddy tendency (Fig. 5d) primarily diffuses momentum along and just inward of V_{\max} . In addition, the vertical eddy tendency primarily acts to reduce momentum along most of near-surface boundary leading to the eyewall (weak blue shading in Fig. 5d outside of V_{\max}). We also note that in Figs. 5c and 5d, the eddy-flux divergences along the V_{\max} contour (blue shading) are accompanied by a momentum “spinup” in the inner edge of V_{\max} toward the eye (red shading) which extends to a height of $\approx 2 \text{ km}$. This spinup extends closer to the surface, by the role of the radial eddy tendencies (Fig. 5c). In a related budget analyses, a similar role of radial eddy tendencies (i.e., their simultaneous “spinup”—“spindown” activity) around V_{\max} was documented by Persing et al. (2013) in both 3D and axisymmetric model configurations. Additionally, Emanuel (1997) showed using a theoretical model that due to the flow transition from the TC eyewall to the eye being strongly frontogenetic (for angular momentum and moist entropy), radial turbulent momentum diffusion at the eye–eyewall interface consequently allows a mechanism for the mechanical spinup of the eye. These patterns from our turbulence-resolving simulation reflect the

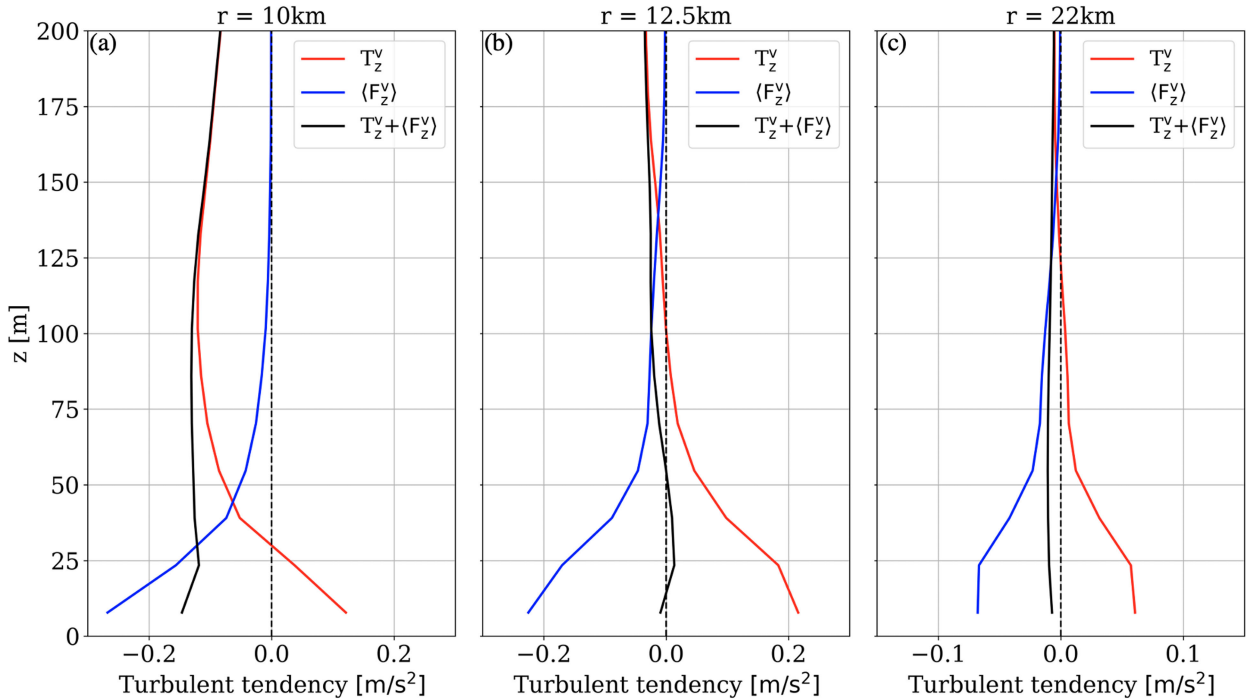


FIG. 6. Profiles for $z = 0\text{--}200$ m, of resolved $[T_z^v]$ (m s^{-2}); red line], parameterized [$\langle F_z^v \rangle$] (m s^{-2}); blue line], and total ($T_z^v + \langle F_z^v \rangle$; black line) turbulent tendencies in the vertical direction for the tangential velocity (shown in Fig. 5d) at (a) $r = 10$, (b) $r = 12.5$, and (c) $r = 22$ km.

diffusion of mean angular velocity (see next subsection) away from its peak and agree with the idea that the spinup of the TC eye and the turbulence-induced diffusive spindown of the eyewall V_{\max} is indeed a feature of TCs (Emanuel 1997; Persing et al. 2013) even in LES.

Curiously, near the surface, there is a weak positive contribution to $\langle v \rangle$ (light red shading in Fig. 5d) just outside of V_{\max} ($r \approx 11\text{--}17$ km) below the height of maximum radial inflow ($z < 50$ m). This weakly positive anomalous tendency suggests a weak enhancement of tangential velocity by turbulent eddies. Figures 6a–c show that, at the inner edge of the eyewall (Fig. 6a) and outside the eyewall (Fig. 6c), the total turbulence tendency (black line) is clearly negative. In contrast, within the eyewall (Fig. 6b), the total turbulence tendency is slightly positive. We do not have a definitive explanation for this feature, although we note that, in a parcel-following (Lagrangian) perspective, the resolved component T_z^v increases notably as parcels near the surface enter the corner-flow region, whereas the subgrid component F_z^v varies smoothly in the same region. This feature might be related to the inhomogeneous conditions, which could violate the assumptions of the surface-layer model, as noted for tornadoes by Wang et al. (2023).

Finally, considering the $\langle w \rangle$ budget, Figs. 5e and 5f show the contribution of the radial and vertical eddy tendencies to the mean flow. The radial eddy tendency (Fig. 5e) is small compared to the vertical eddy tendency (Fig. 5f) which is significantly negative in the lowest region of the inner eyewall and roughly balances the sum of the buoyancy contribution and the vertical gradient of the normalized pressure term (see Fig. A3). The vertical eddy tendency acts to diminish the strength of the mean

upward flow of the vertical velocity in the eyewall. In other words, it opposes the mean eyewall updraft, reducing the magnitude of mean vertical velocity near the surface in the eyewall.

The foregoing analysis indicates that the net effect of the turbulent eddy tendencies in the eyewall region is essentially diffusive in nature—acting to reduce V_{\max} and weaken the strength of the radial inflow close to the surface, as well as the upward flow of air in the eyewall. We also find, from the magnitude and spatial distribution of the eddy tendency terms in the budget equations, that the turbulence tendencies in the vertical direction ($T_z^{u/v/w} + \langle F_z^{u/v/w} \rangle$, i.e., Figs. 5b–f) are generally larger and more spatially prevalent in most of the simulated HBL than those in the radial direction ($T_r^{u/v/w} + \langle F_r^{u/v/w} \rangle$ i.e., Figs. 5a–e), consistent with conventional boundary layer theory. In the localized region around $r \approx 11$ km, however, the radial tendencies ($T_r^{u/v} + \langle F_r^{u/v} \rangle$) become comparable in magnitude to the vertical ($T_z^{u/v} + \langle F_z^{u/v} \rangle$) in terms of their influence on the mean field. In other words, in the inflowing boundary layer (Fig. 4d), the turbulence plays a role similar to a typical PBL, while in the eyewall a more complex picture emerges. The role of turbulent eddies in the mean budget analyses carried out in this study is qualitatively similar to the findings from a similar budget analysis for a tornado by Nolan et al. (2017).

c. The validity of the eddy viscosity hypothesis and estimates of effective mixing lengths

Now that we have established that the turbulence tendencies primarily act to diffuse the mean momentum fields, we now examine a simple turbulence parameterization of eddy fluxes in

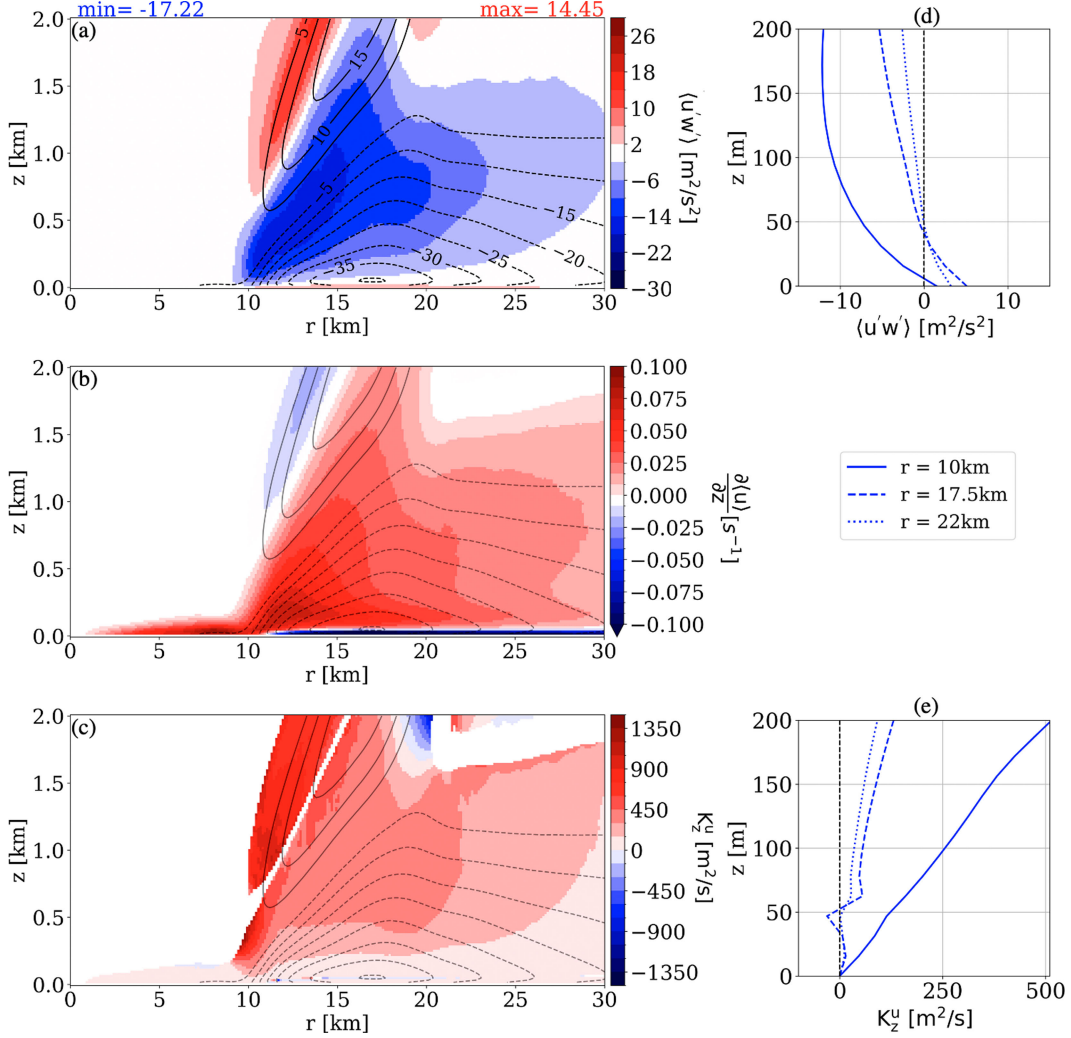


FIG. 7. Contour plots of mean radial velocity $\langle u \rangle$ (m s^{-1}), overlain by shadings of (a) azimuthally and time-averaged vertical fluxes of radial velocity $\langle u'w' \rangle$ ($\text{m}^2 \text{s}^{-2}$), (b) the vertical gradient of mean radial velocity $\partial \langle u \rangle / \partial z$ (s^{-1}), and (c) the effective eddy viscosity K_z^u ($\text{m}^2 \text{s}^{-1}$). [Plots (b) and (c) use the same contour interval for $\langle u \rangle$ as in (a)]. Near-surface profiles of (d) $\langle u'w' \rangle$ and (e) K_z^u for the first 200-m height, at $r = 10$ km (solid blue line), $r = 17.5$ km (dashed blue line), and $r = 22$ km (dotted blue line).

the hurricane boundary layer. As a consequence of their relatively coarse resolution (>1 km), operational weather forecast models must parameterize the role of turbulence. Traditionally, using the molecular diffusion analogies for the eddy fluxes (Anthes 1974; RE87; Stull 1988), the downgradient hypothesis is assumed for the unresolved momentum fluxes. In principle, each flux term can be parameterized by its own eddy viscosity as shown in (4)–(6), where K_z^u , K_z^v are effective eddy viscosities for vertical fluxes of u and v and K_h is an effective eddy viscosity for the $\langle u'v' \rangle$ term:

$$\langle u'w' \rangle \approx -K_z^u \frac{\partial \langle u \rangle}{\partial z}, \quad (4)$$

$$\langle v'w' \rangle \approx -K_z^v \frac{\partial \langle v \rangle}{\partial z}, \quad (5)$$

$$\langle u'v' \rangle \approx -K_h r \frac{\partial \langle v \rangle}{\partial r} \frac{r}{\langle u \rangle}. \quad (6)$$

Since the eddy viscosity is indicative of the “strength” of mixing, it plays a role in the qualitative description of turbulence intensity in the HBL. Here, we evaluate the validity of the widely used downgradient hypothesis, namely, whether or not it leads to nonphysical negative values of the eddy viscosity. [It should be noted that in the fluxes ($\langle u'w' \rangle$, $\langle v'w' \rangle$, and $\langle u'v' \rangle$) discussed below, both the resolved and subgrid flux components—which is only significant in the lowest model levels—are combined and presented.]

Figure 7a shows the vertical flux of radial velocity $\langle u'w' \rangle$ (shaded) and mean radial velocity $\langle u \rangle$ (black contours). The vertical flux $\langle u'w' \rangle$ is generally negative in most of the hurricane

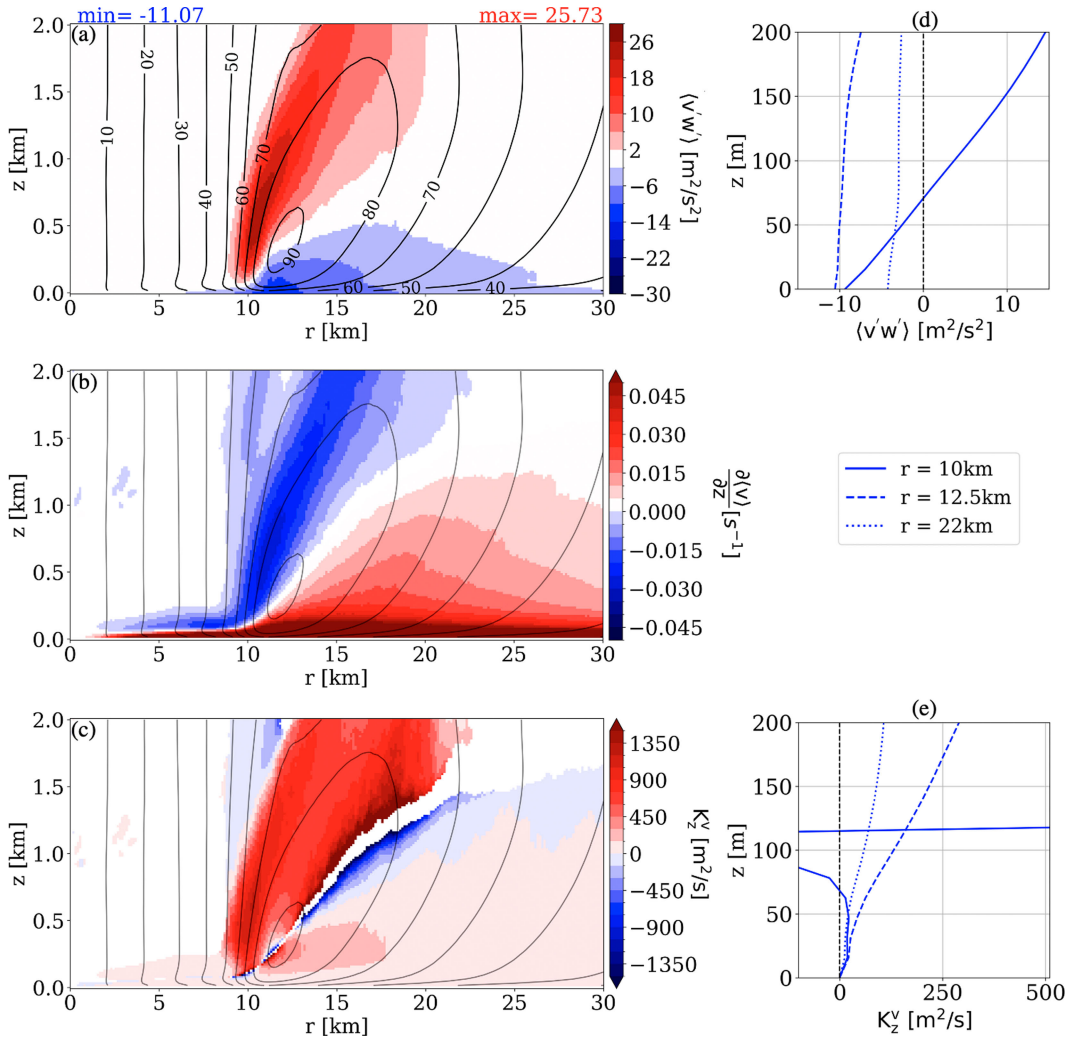


FIG. 8. Contour plots of mean tangential velocity $\langle v \rangle$ (m s^{-1}), overlain by shadings of (a) azimuthally and time-averaged vertical fluxes of tangential velocity $\langle v'w' \rangle$ ($\text{m}^2 \text{s}^{-2}$), (b) the vertical gradient of mean tangential velocity $\partial \langle v \rangle / \partial z$ (s^{-1}), and (c) the effective eddy viscosity, K_z^u ($\text{m}^2 \text{s}^{-1}$). [Plots (b) and (c) use the same contour interval for $\langle v \rangle$ as in (a)]. Near-surface profiles of (d) $\langle v'w' \rangle$ and (e) K_z^u for the first 200-m height, at $r \approx 10 \text{ km}$ (solid blue line), $r \approx 12.5 \text{ km}$ (dashed blue line), and $r \approx 22 \text{ km}$ (dotted blue line).

boundary layer and at most radii (apart from close to the surface and aloft in the inner eyewall, $z \geq 700 \text{ m}$ and $r \approx 11 \text{ km}$). The negative-flux region collocates with regions of positive vertical gradient in radial velocity (Fig. 7b), while the regions of positive fluxes close to the surface coincide with negative gradients, suggesting the downgradient hypothesis is indeed valid. To show this relation more clearly, the effective eddy viscosity $K_z^u = -\langle u'w' \rangle / (\partial \langle u \rangle / \partial z)$ is plotted in Fig. 7c, showing positive values in most of the TC boundary layer, indicative of downgradient turbulent transport. A thin region of negative K_z^u is seen at the top of the inflow BL at about $r \approx 20 \text{ km}$, close to the weak gradient, $\partial \langle u \rangle / \partial z \approx 0$, zone in Fig. 7b. We note that in computing K_z^u , gradients which are less than 3% of the maximum $|\partial \langle u \rangle / \partial z|$ are excluded because the downgradient hypothesis is not applicable in regions with near-zero mean gradients, which would lead to nonphysically large-eddy viscosity

values. Figures 7d and 7e show near-surface profiles of $\langle u'w' \rangle$ and K_z^u , respectively, at specific radii of interest. From Fig. 7d (at $r \approx 17.5 \text{ km}$ and $r \approx 22 \text{ km}$), weakly positive vertical momentum flux is seen below the height of maximum radial inflow ($z < 50 \text{ m}$). Just above, near the level of maximum inflow where the mean gradient is small, Fig. 7e indicates a weak region of countergradient flux denoted by negative K_z^u . In contrast, the profile at $r \approx 10 \text{ km}$ (solid blue lines in both Figs. 7d,e) shows a steady increase of $\langle u'w' \rangle$ and K_z^u with height, with K_z^u staying positive, as this profile was located slightly inwards of the eyewall where the maximum value of inflow is at the surface.

For the vertical flux of tangential velocity $\langle v'w' \rangle$, Fig. 8a shows that negative values at the lower heights ($z \leq 500 \text{ m}$) correspond to regions of positive vertical gradients (Fig. 8b), while positive-flux values are generally associated with the negative gradients where there is outflow above the boundary

layer. Plotting $K_z^v = -\langle v'w' \rangle / (\partial \langle v \rangle / \partial z)$ in Fig. 8c, again the downgradient hypothesis is seen to be valid for most of the HBL, except for a narrow band of negative eddy viscosity (countergradient flux) which extends from the inner eyewall to a radius of ≈ 30 km. Again, mean gradients $< 3\%$ of $\max |\partial \langle v \rangle / \partial z|$ are excluded here. A closer look at the vertical gradient field $\partial \langle v \rangle / \partial z$ shown in Fig. 8b indicates that this region of countergradient flux (seen in Fig. 8c) coincides with a region of comparatively weak vertical velocity gradient of tangential velocity along the inflow boundary, similar to the results for radial velocity above. Figures 8d and 8e show near-surface profiles of $\langle v'w' \rangle$ and K_z^v , respectively, at specific radii of interest ($r = 10, 12.5$ and 22 km). The height of countergradient flux (i.e., negative K_z^v) at $r = 10$ km (solid blue line in Fig. 8e) corresponds to the height where the mean velocity gradient (Fig. 8b) transitions from positive to negative, similar to the behavior seen in K_z^u above, at $r = 17.5$ km and $r = 22$ km (Fig. 7e).

These results highlight that, although the downgradient hypothesis is largely valid in the HBL according to this simulation, regions near weak mean gradients can be problematic. This is in agreement with a recent LES study in sheared environments by Wang and Jiang (2017), where countergradient fluxes of $\langle v'w' \rangle$ near the top of the HBL were associated with a weak vertical gradient in the tangential velocity. We note, however, that regions of countergradient fluxes in Figs. 7c and 8c correspond to regions where the contributions of the turbulent tendencies (T_z^u and T_z^v) to the mean-field budgets in Figs. 5b and 5d, respectively, are not substantial, suggesting that downgradient diffusion is sufficient for parameterization of the inner core of strong hurricanes. Of course, further analysis is needed with different types of storms (e.g., larger, weaker, and sheared) to test the robustness of this conclusion.

This analysis of K_z^u and K_z^v helps clarify vertical turbulent flux distribution in and around the TC eyewall, where the flow becomes complex near the corner-flow region. For PBL parameterizations, however, consolidating K_z^u and K_z^v into one effective eddy viscosity for momentum fields is common practice, in order to reduce the number of parameters. To characterize this type of effective eddy viscosity, we use the following equation:

$$K_{\text{eff}}^v = \frac{\sqrt{\langle u'w' \rangle^2 + \langle v'w' \rangle^2}}{\sqrt{(\partial \langle u \rangle / \partial z)^2 + (\partial \langle v \rangle / \partial z)^2}}. \quad (7)$$

The spatial pattern of K_{eff}^v in Fig. 9 shows that the strongest turbulence is along the inner edge of the eyewall ($r \approx 10$ km), with values as high as $\approx 1000 \text{ m}^2 \text{ s}^{-1}$. A vertical profile of K_{eff}^v at this location is shown in Fig. 9b, indicating eddy diffusivity values exceeding $1000 \text{ m}^2 \text{ s}^{-1}$ at $z \approx 500$ m, with values $\approx 250 \text{ m}^2 \text{ s}^{-1}$ for $z > 1.5$ km in the eyewall. The high K_{eff}^v in this region (the corner flow) is likely explained by the inhomogeneous conditions here, evident in the sharp deceleration of the radial inflow accompanied by increasing vertical velocity. Horizontal velocity gradients, as well as the mean vertical velocity field, are typically assumed to be negligible in boundary layer parameterizations, but in the eyewall of TCs, they play a substantial role in the generation of TKE (not shown).

Outside the eyewall ($r \approx 22$ km), the vertical profile in Fig. 9c shows a steady increase of K_{eff}^v from the surface to about $z \approx 500$ m, after which K_{eff}^v stays nearly constant with height at a value of $\approx 300 \text{ m}^2 \text{ s}^{-1}$. In both Figs. 9b and 9c, the insets show that K_m (the standard subgrid-scale eddy viscosity model) and K_w (the two-part near-wall subgrid model) are only nonnegligible in the lowest few model levels.

The mean values for eddy viscosity (≈ 40 – $130 \text{ m}^2 \text{ s}^{-1}$) reported by Zhang et al. (2010) using a ≈ 450 -m flight-level dataset through the intense eyewall of two category 4/5 storms are similar to the values ($\leq 180 \text{ m}^2 \text{ s}^{-1}$) found in the present study, at a similar height ($z \leq 0.5$ km) just outside the eyewall (Fig. 9c). A similar observational study by Sparks et al. (2019) using aircraft data from eyewall penetrations of four TCs (at ≈ 600 – 650 m height) found effective vertical eddy viscosity $> 200 \text{ m}^2 \text{ s}^{-1}$ in the eyewall region, well within the range of values seen in the present study.

Zhang and Drennan (2012) computed the vertical distribution of eddy diffusivities from observations, using in situ aircraft data collected during four intense storms. In their study, using data collected during the Coupled Boundary Layers Air–Sea Transfer (CBLAST) Defense Research Initiative field campaign (Black et al. 2007; French et al. 2007; Drennan et al. 2007), they found no clear evidence of countergradient momentum fluxes. We however note that the data used in their study were far from the storm center, in the outer rainband region of the storms. The analysis presented in this study focuses on the eyewall/inflow BL region of the storm. Additional flights (possibly using unmanned aircraft) into the most-turbulent regions of the storm at low altitude are needed to further confirm the validity of the downgradient eddy viscosity hypothesis for momentum fluxes in the inner core of hurricanes.

Going further, simple parameterizations for eddy diffusivity often use a mixing length l , e.g.,

$$K_v = l^2 |S_v|, \quad (8)$$

following the Smagorinsky formulation (Smagorinsky 1963), where S_v is the deformation (also see Tennekes and Lumley 1972, p. 49). (The effects of buoyancy are neglected for simplicity.) Having highlighted the distribution of effective eddy viscosity, we proceed with investigating the spatial distribution of the effective vertical mixing length L_{eff}^v in the tropical cyclone BL.

We begin first by computing the effective mixing length using (8) and substituting the effective eddy viscosity (7) for the lhs:

$$L_{\text{eff}}^v = \left[K_{\text{eff}}^v / \sqrt{(\partial \langle u \rangle / \partial z)^2 + (\partial \langle v \rangle / \partial z)^2} \right]^{1/2}. \quad (9)$$

The result (Fig. 10a) shows that at $r > 11$ km, L_{eff}^v increases monotonically with height from 0 at the surface to ≈ 100 m from 1 km above the surface. A vertical profile of L_{eff}^v taken at $r = 10$ km is shown in Fig. 10b, revealing a nonmonotonic behavior with height, and relatively high values of L_{eff}^v (≈ 300 m) between $z \approx 500$ and 1000 m. On the other hand, a vertical profile of L_{eff}^v at $r = 22$ km, shown in Fig. 10c, indicates that the effective mixing length increases more slowly and monotonically from ≈ 0 m at the surface to about ≈ 100 m at $z \approx 500$ m, where

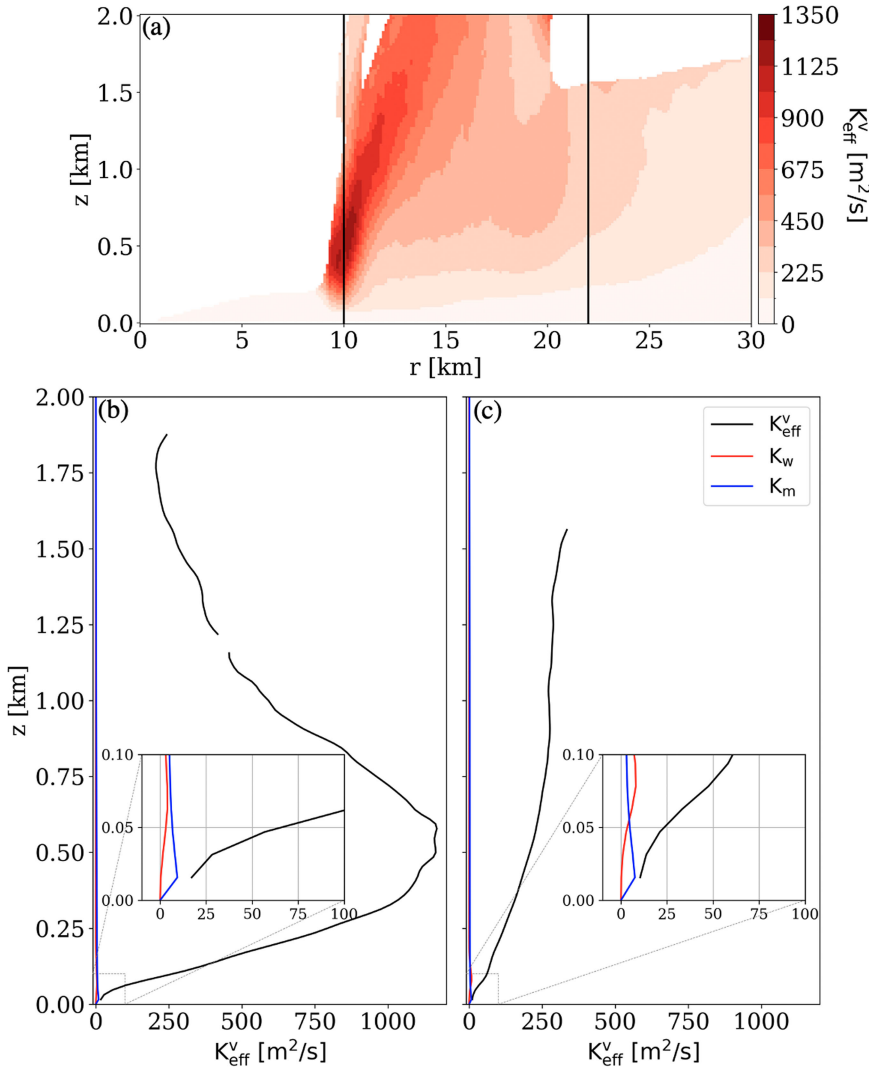


FIG. 9. (a) Plot of effective eddy viscosity K_{eff}^v ($\text{m}^2 \text{s}^{-1}$). Vertical profiles of K_{eff}^v (black line), K_w (red line), and K_m (blue line) at (b) $r \approx 10$ km and (c) $r \approx 22$ km. [The black vertical lines in (a) indicate the radii where the black profiles in (b) and (c) are plotted.] The insets in (b) and (c) show windowed-in plots of the first 100-m height of the BL.

it remains constant with height up until $z \approx 1$ km. Above $z \approx 1000$ m, at the location of this vertical profile, the value of L_{eff}^v increases sharply (possibly due to the decreasing vertical wind shear at the exact same location seen in Figs. 7b and 8b) until it becomes undefined. This region also coincides with the top of the inflow layer (Fig. 4b). The range (≈ 35 – 55 m) of L_{eff}^v estimated by Zhang and Drennan (2012) is comparatively smaller (about half) of the LES-derived values from outside the eyewall ($r \approx 22$ km and $0 \text{ km} \leq z \geq 1.0 \text{ km}$ – Fig. 10c) in the present study, most likely due to the relatively low surface wind regime (18 – 30 m s^{-1}) between the TC outer rainbands where their data were collected. Zhang et al. (2010) estimated vertical mixing lengths of ≈ 100 m in the eyewall region of Hurricane Hugo (1989) and Allen (1980) at ≈ 450 – 500 -m flight height. The L_{eff}^v from our study, in the eyewall region (see Fig. 10a), agrees

well with the observational estimates by Zhang et al. (2010). We also note that Zhang et al. (2010) documented, with some caveats [i.e., including flight segment cutting through the eyewall vorticity maxima (EVM)], vertical mixing length of ≈ 220 m from eyewall-penetrating flight legs into Hurricane Hugo (1989). The L_{eff}^v from our study indeed approaches and exceeds ≈ 220 m at the inner edge of the eyewall. In this sense, the present study provides guidance on the vertical and horizontal distribution of L_{eff}^v in the most intense region of the TC environment.

Various analytical estimates of L_{eff}^v have been formulated and employed in the parameterization of TC boundary layer behavior (Blackadar 1962; Louis 1979; Mason and Thomson 1992; Bryan and Rotunno 2009; Kepert 2012). A widely used PBL model, the Louis scheme, often uses the formulation in (10) and is based on Blackadar (1962):

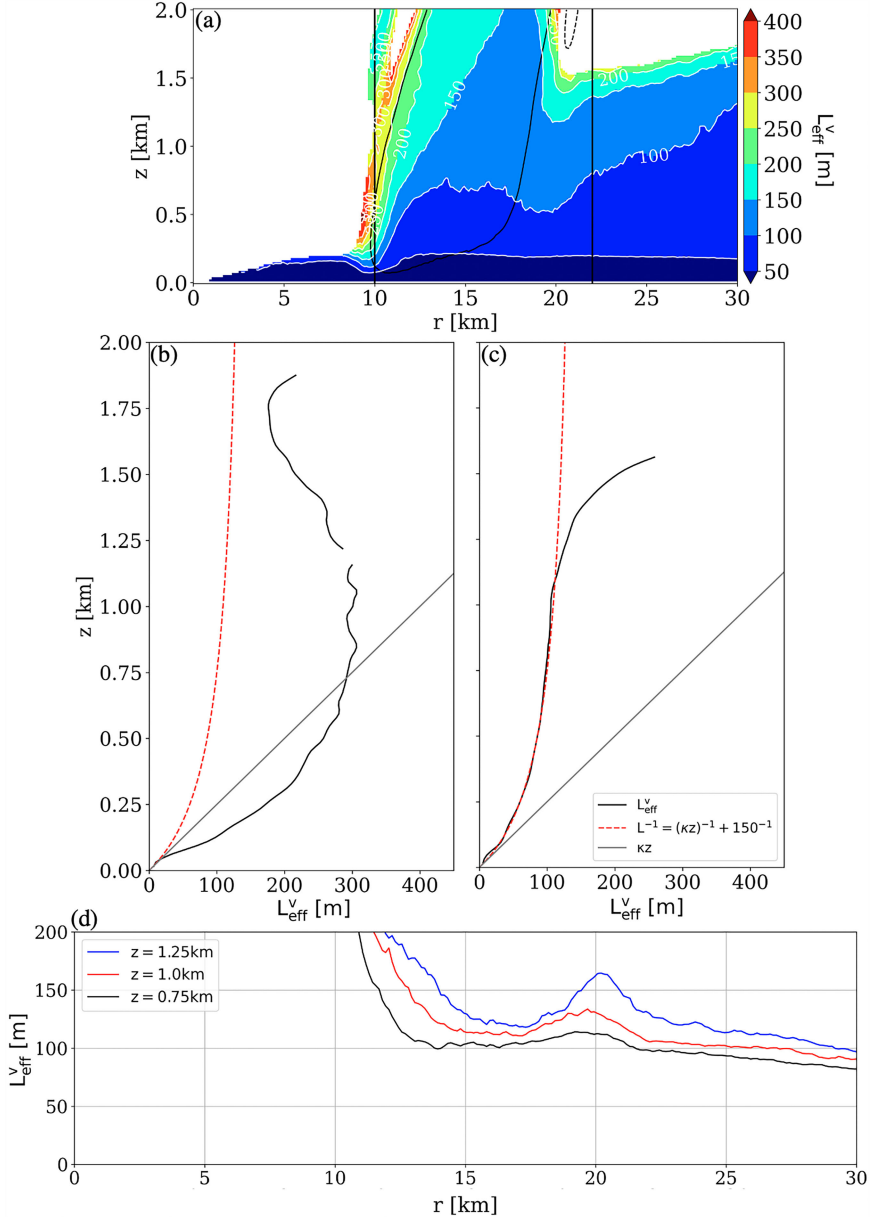


FIG. 10. Plots of the effective mixing length L_{eff}^v (m). (a) Radius–height plot. (b),(c) Vertical profiles of L_{eff}^v (black line) and analytical Louis-type profiles (red dashed lines; with $L_\infty = 150$ m) and the Prandtl theoretical surface layer relations (gray line) at (b) $r = 10$ km and (c) $r = 22$ km. (d) Radial variation of L_{eff}^v at $z = 0.75, 1.0$, and 1.25 km (black, red, and blue lines, respectively). [The black vertical lines in (a) indicate the locations of the profiles in (b) and (c). The solid and dashed black contours in (a) indicate $\langle w \rangle$ at ± 1.0 m s $^{-1}$.]

$$\frac{1}{L} = \frac{1}{\kappa z} + \frac{1}{L_\infty}, \quad (10)$$

where κ and L_∞ represent the von Kármán constant (≈ 0.4) and the asymptotic length scale (prescribed by the user), respectively.

In Fig. 10c, we find that the analytical formulation using $L_\infty = 150$ m (red dashed line) captures well the vertical

variation of the effective mixing length L_{eff}^v outside the eye-wall, from the surface to $z \approx 1000$ m. Interestingly, this same value (≈ 150 m) for L_∞ was recommended in one of the earliest reformulations of the Louis scheme (Louis et al. 1982). In their study, Zhang and Drennan (2012) found that a large number of estimated L_∞ values fall between 40 and 80 m—also about half of $L_\infty = 150$ m seen to be a reasonable fit in the present study at $r \approx 22$ km (Fig. 10c)—although a few

values as high as ≈ 140 m were found. This discrepancy between our results and Zhang and Drennan (2012) could be a consequence of multiple factors, including the sample size used in their study and the intensity of different storms on which the analyses were based as well as the proximity to the intense eyewall region. A comparison of the Prandtl theoretical surface layer relation, Prandtl (1932) (gray line in Fig. 10c) and the model computed L_{eff}^v (black line), indicates that the simulation roughly captures the behavior of the theory very close to the ground—an expected behavior widely seen in simple boundary layer flows (Rossby and Montgomery 1935; Schlichting and Kestin 1961; Blackadar 1962; Biswas and Eswaran 2002)—above which the model-derived value approaches an asymptotic value.

However, in the inner eyewall (Fig. 10b), the Louis scheme profile with $L_\infty \approx 150$ m does not capture the vertical variation of L_{eff}^v found in the present study, even qualitatively. The L_{eff}^v from the present study (black solid line) is consistently higher than the analytical profile across most of the BL height, suggesting that the widely used asymptotic formulation of the effective mixing length [(10)] underpredicts the magnitude of the effective mixing length in the most intense regions of the TC. Furthermore, unlike outside the eyewall (Fig. 10c), L_{eff}^v seen here is notably larger than the Prandtl surface layer relation (gray line) as z increases from the ground up until $z \approx 0.75$ km. These results suggest that the nature of turbulence in the corner flow of the TC eyewall may be fundamentally distinct from traditional boundary layer turbulence. We suspect that contributions from horizontal gradients, which can be quite strong in hurricane eyewalls but are neglected in traditional boundary layer equations, are probably responsible for these different results in the corner-flow region.

Figure 10d shows the radial variation of L_{eff}^v at $z = 0.75, 1.0$, and 1.25 km (black, red, and blue solid lines, respectively). At all heights, outside the eyewall ($r > 20$ km), L_{eff}^v is seen to decrease steadily with increasing radii, with values generally less than 120 m. In the inner half of the eyewall ($r < 15$ km), however, L_{eff}^v increases rapidly with decreasing radii. This sharp increase in the magnitude of L_{eff}^v in the corner-flow region is again attributed to the nontraditional behavior of turbulence in this region relative to the inflowing boundary layer. The local peak in the values of L_{eff}^v at $r = 20$ km appears to be associated with the downdraft feature (dashed black contour in Fig. 10a).

In most boundary layer parameterization schemes, the horizontal momentum flux $\langle u'v' \rangle$ is assumed to be smaller than the vertical momentum fluxes $\langle u'w' \rangle$ and $\langle v'w' \rangle$ (e.g., Malkus and Riehl 1960). However, in the corner-flow region of the storm, Zhang and Montgomery (2012) suggest that horizontal mixing may become just as important as vertical mixing in terms of its effect on the vortex dynamics (this is confirmed in the analyses of the flux divergences presented in Fig. 5). Bryan and Rotunno (2009), Rotunno and Bryan (2012), and Bryan (2012) pointed out the importance of horizontal momentum diffusion and associated mixing lengths on the maximum intensity of simulated storms. Comparing Fig. 11a to Figs. 7a and 8a, it is seen that in the corner-flow region, the horizontal momentum flux is significantly (≈ 3 times)

greater than the vertical momentum fluxes. Figures 11a and 11b also show that regions of positive horizontal momentum flux correspond to regions of negative radial gradient [$[r(\partial/\partial r)(\langle v \rangle/r)]$], again confirming mostly downgradient transport of horizontal momentum.

Interestingly, a plot of the effective radial eddy viscosity $[K_h = -(\langle u'v' \rangle/r)(\partial/\partial r)(\langle v \rangle/r)]$ in Fig. 11c shows that the regions of countergradient fluxes (blue shading; negative values of eddy viscosity) are located close to the surface region ($z \leq 100$ m) and near the inner edge of the eyewall ($r \approx 10$ – 11 km), extending up to the top of the boundary layer ($z \approx 2$ km). For the near-surface region, where the magnitude of negative eddy viscosity is comparatively smaller, the countergradient fluxes are clearly seen to be below the height of maximum radial inflow (black dashed contour in Fig. 7a) where momentum is most likely being lost to the surface due to friction. For the region near the inner edge of the eyewall, however, the countergradient flux signatures do not entirely coincide with weak radial gradient zones and are comparatively significant in magnitude and spatial extent at the top of the BL. Again, we note that the contributions of the turbulent tendency to the mean flow (Fig. 5c) around the region where the countergradient fluxes are found here are not substantial and thus may not significantly influence the storm mean wind field. A closer look at the mean radial velocity field (black contour in Fig. 7a) reveals that this region of countergradient flux at the top of the BL actually coincides with the outflow region. This result would imply that the countergradient fluxes seen in this region (Fig. 11c) may be related to large eddies that span the interface between the weak negative inflow region and the outflow at the top of the HBL. Furthermore, the countergradient flux signatures slightly inwards of the inner edge of the eyewall ($r < 10$ km), extending from the surface to top of the BL, could also be related to large eddies at inner edge of the eyewall (Fig. 3a).

A comparison of the magnitudes of K_h with K_z^u and K_z^v in Figs. 7c, 8c, and 11c, respectively, suggests the anisotropic nature of turbulence processes in the corner-flow region of a TC. The values of K_h found in the present study are similar to the observation measurements (≈ 1500 $\text{m}^2 \text{s}^{-1}$) recorded by Zhang and Montgomery (2012) using aircraft measurements flown at about ≈ 500 -m height into the eyewall of three intense storms [category 5, Hurricane David (1979); category 4, Hurricane Allen (1980); and category 5, Hurricane Hugo (1989)]. This result confirms the importance of horizontal diffusion in the corner-flow region of the hurricane boundary layer, supporting the findings from previous observational (Zhang and Montgomery 2012) and numerical (Bryan and Rotunno 2009; Bryan 2012; Zhang and Marks 2015) studies.

In summary, the downgradient eddy viscosity hypothesis is valid in most of the boundary layer according to this simulation, although regions of countergradient fluxes are noted in regions of weak gradient near the eyewall and inflow layer top. The magnitude and spatial distribution of K_h also indicate that the downgradient hypothesis is largely valid, except for certain regions within the eyewall. That said, in the context of the turbulence tendencies (shown in Fig. 5), we find that these countergradient regions may not actually significantly alter the

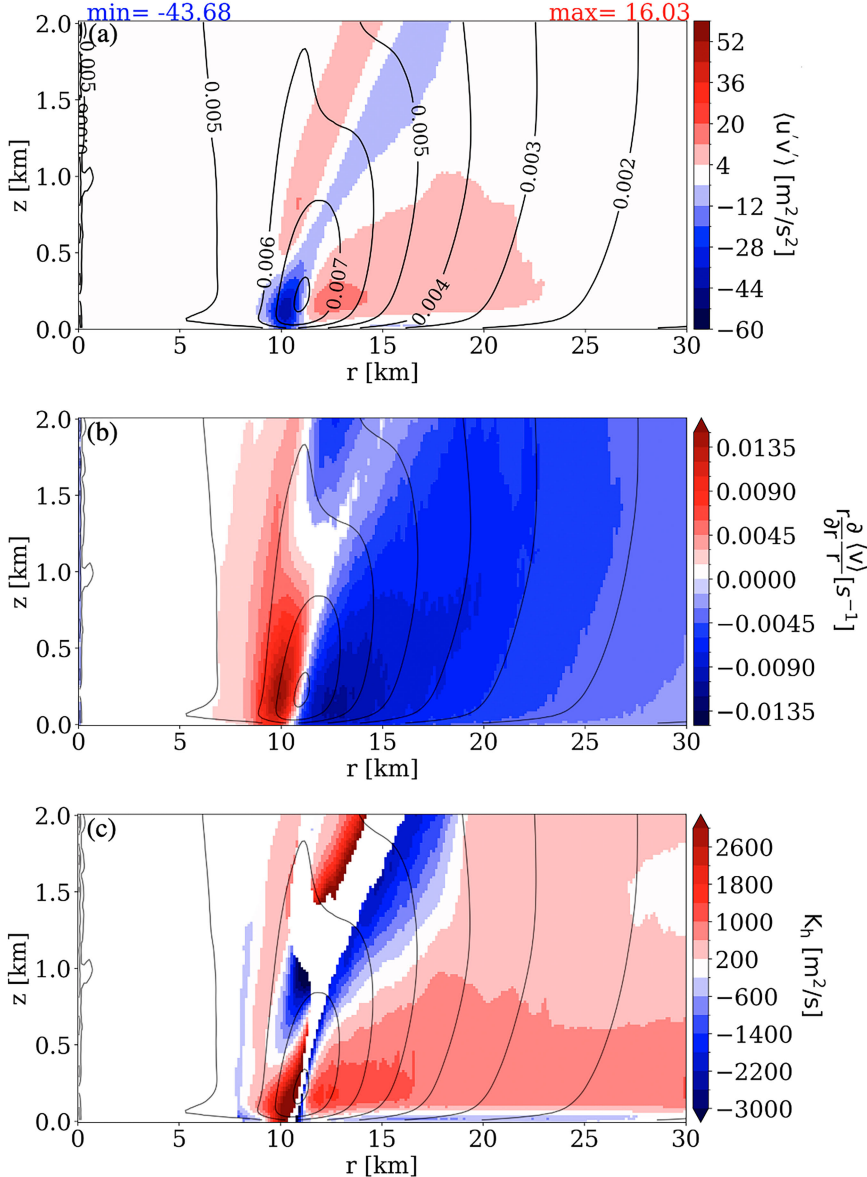


FIG. 11. Contour plots of $\langle v' \rangle / r$ (s^{-1}), overlain by shadings of (a) azimuthally and time-averaged radial fluxes of tangential velocity $\langle u'v' \rangle$ ($\text{m}^2 \text{s}^{-2}$), (b) $r \times$ the radial gradient of rotation rate $r(\partial/\partial r)(\langle v' \rangle / r)$ (s^{-1}), and (c) the effective eddy viscosity K_h ($\text{m}^2 \text{s}^{-1}$). [Plots (b) and (c) use the same contour interval for $\langle v' \rangle / r$ as in (a).]

mean fields. A more systematic study of countergradient fluxes in the HBL [possibly using higher-order closure models (e.g., Nardi et al. 2022) or mass-flux schemes (Han and Bretherton 2019; Chen and Marks 2024)], in addition to novel high-resolution observations, would be needed to further clarify this conclusion.

d. A revised formulation of eddy viscosities

The simple parameterization of radial flux (6) only considers the shear stress term $\langle u'v' \rangle$. However, (1)–(3) indicate that this is not the only turbulent stress term acting in the radial direction (see Fig. 5a)—terms containing $\langle u'^2 \rangle$ and $\langle v'^2 \rangle$

also influence the mean flow. Thus, the eddy viscosity K_h shown previously in Fig. 11 only accounts for a portion of the radial turbulence transport. A similar approximation was made by Zhang and Montgomery (2012).

In their axisymmetric numerical model, RE87 developed and presented relationships for separate eddy viscosities in the radial and vertical directions. They noted following Mason and Sykes (1982) that having a significantly larger horizontal grid spacing (compared to the vertical) necessitates the need for different parameterizations in these two directions in mesoscale models. In the present study, with the turbulent stresses mostly resolved in the corner-flow region (and the

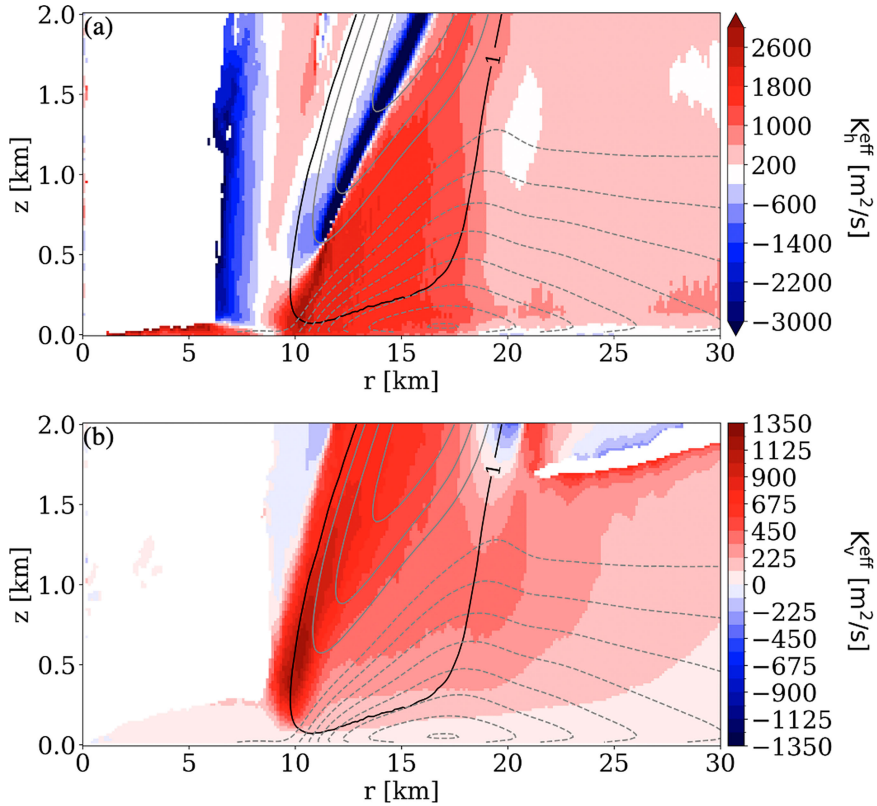


FIG. 12. Plots of (a) effective radial eddy viscosity K_{eff}^h ($\text{m}^2 \text{s}^{-1}$) using (14) and (b) effective vertical eddy viscosity K_{eff}^v ($\text{m}^2 \text{s}^{-1}$) using (15). The solid black contour line in each panel indicates $\langle w \rangle$ of $+1.0 \text{ m s}^{-1}$, highlighting the eyewall region. The solid and dashed gray contour lines in each panel show the mean radial velocity $\langle u \rangle$, using the same contour interval as in Fig. 7a.

horizontal grid spacing being similar to the vertical), we can evaluate their formulations for an effective radial eddy viscosity which includes all components of the Reynolds stresses relevant to mixing in the radial direction.

Following RE87 (p. 545), we form a turbulent kinetic energy equation assuming equilibrium conditions, i.e., a balance between production and dissipation. For the radial direction, we have

$$-\langle u' v' \rangle r \frac{\partial \langle v \rangle}{\partial r} - \langle u'^2 \rangle \frac{\partial \langle u \rangle}{\partial r} - \langle v'^2 \rangle \frac{\langle u \rangle}{r} - \langle w'^2 \rangle \frac{\partial \langle w \rangle}{\partial z} = \epsilon. \quad (11)$$

The production terms [lhs of (11)] are essentially the same as those leading to RE87's Eq. (29), except for two important differences: 1) we do not invoke any parameterization for the Reynolds stresses and 2) we include a term with $\partial \langle w \rangle / \partial z$, which is needed for consistency in the complete stress tensor (e.g., Wajcikowicz 1993).

Next, as in RE87, we assume based on dimensional grounds that dissipation has the form

$$\epsilon = (K_{\text{eff}}^h)^3 / l_h^4, \quad (12)$$

where K_{eff}^h is an effective eddy viscosity in the radial direction and l_h is an associated effective length scale. Further, we

assume l_h is related to K_{eff}^h and the horizontal deformation S_h via a traditional "Smagorinsky" model,

$$K_{\text{eff}}^h = l_h^2 S_h, \quad (13)$$

where $S_h^2 = [r(\partial/\partial r)(\langle v \rangle/r)]^2 + 2[(\partial \langle u \rangle / \partial r)^2 + (\langle u \rangle/r)^2 + (\partial \langle w \rangle / \partial z)^2]$. Using (13) to eliminate l_h from (12), the resulting equation for the rhs of (11) leads to a relation for effective horizontal eddy viscosity:

$$K_{\text{eff}}^h = \frac{\left(-\langle u' v' \rangle r \frac{\partial \langle v \rangle}{\partial r} - \langle u'^2 \rangle \frac{\partial \langle u \rangle}{\partial r} - \langle v'^2 \rangle \frac{\langle u \rangle}{r} - \langle w'^2 \rangle \frac{\partial \langle w \rangle}{\partial z} \right)}{\left[r \left(\frac{\partial \langle v \rangle}{\partial r} \right)^2 + 2 \left(\frac{\partial \langle u \rangle}{\partial r} \right)^2 + 2 \left(\frac{\langle u \rangle}{r} \right)^2 + 2 \left(\frac{\partial \langle w \rangle}{\partial z} \right)^2 \right]}. \quad (14)$$

This formulation now includes contributions from all terms associated with turbulence tendencies in the radial direction. It reduces to (6) if all terms except those with $\langle u' v' \rangle$ and $r(\partial/\partial r)(\langle v \rangle/r)$ are neglected.

Figure 12a shows a plot of K_{eff}^h determined using (14). This result is much less complicated than that shown in Fig. 11c, particularly in the eyewall. Figure 12a also shows that the downgradient eddy viscosity hypothesis is valid for most of

the HBL, except in two thin regions: within the eye (where the blue shading extends from the surface to the top of the plot) and within the inner edge of the eyewall for $z > 500$ m. For the region in the eye, the countergradient radial flux region has negligible effect on the mean flow, since the turbulent tendencies there are so small (Fig. 5). We also note that the location and scale of the countergradient flux signature seen in the eye suggest that they are possibly related to the coherent turbulent structures seen in Figs. 2 and 3 and in a recent work by Protzko et al. (2023). For the eyewall, the countergradient fluxes seem to reside above the inflow layer (dashed gray contour lines) and may be related to the transition from an inflowing to outflowing flow pattern in the TC eyewall; in other words, there may be a turbulence “memory” effect [see Hinze (1976)] as air parcels move through the corner-flow region.

Following a similar procedure, an effective eddy viscosity in the vertical direction can be derived:

$$K_{\text{eff}}^v = \frac{\left(-\langle u'w' \rangle \frac{\partial \langle u \rangle}{\partial z} - \langle v'w' \rangle \frac{\partial \langle v \rangle}{\partial z} \right)}{\left[\left(\frac{\partial \langle u \rangle}{\partial z} \right)^2 + \left(\frac{\partial \langle v \rangle}{\partial z} \right)^2 \right]}. \quad (15)$$

The result, shown in Fig. 12b, is quite similar to the previous result (shown in Fig. 9a), except that this newer formulation allows for the existence of countergradient flux regions. Furthermore, the magnitudes of both formulations are quite similar (with the Fig. 9a being slightly higher). From Fig. 12b, the downgradient eddy viscosity hypothesis is again seen to be valid in most of the BL, while small regions of countergradient flux signatures are seen above the inflowing BL, outside the eyewall and slightly inward of the inner eyewall ($z \geq 1$ km).

4. Conclusions and discussion

Turbulence in the inner core of an idealized category 5 Hurricane is analyzed using large-eddy simulation (LES) model output with a horizontal grid size of 31.25 m. Intense updrafts/downdrafts with vertical scales of $\approx 1.5\text{--}2.5$ km, similar to those seen in research flight missions into intense category 4/5 storms, are ubiquitous at the inner edge of the eyewall, decreasing in vertical extent with radial distance from the storm center. The role of turbulence on the mean momentum fields is shown to be primarily downgradient in nature. Azimuthally and time-averaged momentum flux provides insights into the nature of turbulent fluxes in the HBL, which are summarized below:

- 1) Turbulent eddy tendencies in the inner core (i.e., eye, eyewall, and nearby rainbands) of intense hurricanes primarily act diffusively on the mean velocity fields, acting to weaken the strength of the eyewall, decreasing the mean radial inflow and the updraft strength in the corner-flow region of the eyewall.
- 2) In most of the HBL, the downgradient hypothesis is valid for vertical and horizontal momentum fluxes $\langle u'w' \rangle$, $\langle v'w' \rangle$, and $\langle u'v' \rangle$. Near the top of the boundary layer, a distinct countergradient region is noted for $\langle v'w' \rangle$ where

the vertical gradient of tangential velocity $\partial \langle v \rangle / \partial z$ is weak. Similarly, for the horizontal momentum flux $\langle u'v' \rangle$, countergradient flux signatures are seen in parts of the eyewall. However, their effect on the mean wind field is minimal, as they are around zones where the relevant turbulent tendencies in the mean budget equations are negligible. We note that the azimuthally averaged results presented in this study apply most directly to axisymmetric models, and thus, applicability to 3D NWP models is unclear.

- 3) Analytical formulations for L_{eff}^v , used in the Louis scheme, are shown to perform well outside the eyewall but underestimates the LES-derived values by about half in the inner edge of the inner eyewall. Additionally, we provide estimates of the effective vertical mixing lengths L_{eff}^v in the most intense regions of TCs.
- 4) A complete formulation of the effective horizontal eddy viscosity (accounting for typically ignored stress terms) is presented, showing the validity of the downgradient eddy viscosity hypothesis in most of the HBL, except along narrow regions in the eye and at the inner edge of the eyewall.

From our findings, we propose a simple conceptual framework for understanding the role of turbulence in the hurricane boundary layer: the mean velocity field brings in air parcels from the outer eyewall, converging in the inner eyewall which acts as a frontal system for angular momentum and entropy (Emanuel 1997). It should be noted that the argument for the frontogenetic nature of the TC eyewall–eye transition was previously suggested by Eliassen (1959) p. 286 and Palmén and Newton (1969) p. 486 but more rigorously shown by Emanuel (1997). In the inner eyewall, we find that turbulent eddies act to diffuse momentum. We show, unambiguously, that turbulence acts to weaken the frontal gradient (eyewall), enhancing mixing into the eye, while simultaneously weakening the strength of radial inflow. The divergence of the turbulent momentum fluxes is more pronounced in the eyewall but is notable in the inflowing boundary layer as well. The complex distribution of effective eddy viscosity in the eyewall re-emphasizes the need for a more complete parameterization of turbulent momentum fluxes in this region for mesoscale forecast models (Rotunno et al. 2009), which should account for horizontal gradients and associated turbulent fluxes [e.g., $\langle u'v' \rangle$, $\langle u'u' \rangle$, and $\langle v'v' \rangle$].

Understanding the magnitude and distribution of turbulent fluxes in the eyewall region and the HBL in general is the subject of ongoing research and remains highly relevant for a better understanding of intensity changes in hurricanes. The recent use of small uncrewed aircraft systems (UAS) in the inner core of intense storms shows great potential in complementing the use of manned-aircraft missions (Cione et al. 2020). Although this study presents results for a single intense TC, we have shown that turbulence (which remains largely parameterized in current weather forecast models) plays a nonnegligible role in the modification of the TC mean wind fields. The role of turbulence on temporarily evolving (i.e., intensifying/weakening) storms remains to be clarified. Possible future research opportunities thus lie in the investigation of

the evolution of TC turbulence under moderate to strong vertical wind shear.

Acknowledgments. We acknowledge useful personal correspondence with Dr. Stephen Guimond and Dr. Ralph Foster. We also acknowledge ONR Grants N00014-19-S-B001 to the University of Notre Dame and N00014-20-1-2071 to NCAR/UCAR for financial support under the Tropical Cyclone Rapid Intensification (TCRI) campaign. George Bryan, Richard Rotunno, and Peter Sullivan were also supported by the NSF under Cooperative Agreement 1852977. We also acknowledge high-performance computing support from Cheyenne (<https://doi.org/10.5065/D6RX99HX>) provided by NSF NCAR's Computational and Information Systems Laboratory. Finally, the corresponding author would like to recognize the NCAR Advanced Study Program (ASP) Graduate Visitor Program (GVP) from which a collaborative research visit to NCAR was supported.

Data availability statement. Due to the large size (several tens of terabytes), the model simulation output used in this study is stored on NSF NCAR's campaign storage system and is available upon request to Dr. George Bryan.

APPENDIX

Mean-Field Budget Analyses

Figure A1 shows the plot for other terms (mean advection terms, centripetal, pressure gradient, and Coriolis force) in the azimuthally and time-averaged budget [(1) and (2)]. For $\langle v \rangle$, the combined effect of the mean advection terms (first two rows) is to transport tangential velocity from the outer eyewall into the inner eyewall V_{\max} and aloft to the eyewall. Comparing this to the centripetal tendency directly below (third row),

it is seen that the advective tendencies play an opposing role to the centripetal. For $\langle u \rangle$, it is seen that the combined effect of the mean advective tendencies (first two rows) is to transport the radial wind speed from outside the maximum inflow region (>15 km) toward the inner eyewall and aloft to the eyewall region. The combined centripetal and pressure gradient tendencies make nearly (but not exactly) compensating opposite contributions, with the net effect of positively contributing to the radial inflow in most regions slightly outside of the eyewall ($r \geq 17$ km) and also within the eyewall (but only beneath the height of maximum radial inflow). In both the $\langle v \rangle$ and $\langle u \rangle$ budgets, the azimuthally and time-averaged Coriolis tendencies contribute insignificantly to the mean budget equation.

For Fig. A2, we see generally that the turbulent tendencies make a comparatively spatially smaller (but significant in magnitude) contribution to the mean budget [(1) and (2)]. In both $\langle v \rangle$ and $\langle u \rangle$, we note that the contributions from the vertical tendencies are comparatively more significant in magnitude, as opposed to radial tendencies. Furthermore, we note that the parameterized vertical tendencies for $\langle v \rangle$ and $\langle u \rangle$ are only significant at the lowest few model levels, with the standard subgrid parameterization term being larger than the two-part term. In the rest of the boundary layer, the resolved turbulence dominates. Comparing Figs. A1 and A2, it is seen that the role of the turbulent eddies is most significant in the eyewall, corner-flow region, and close to the surface.

Figure A3 shows plots of the mean and turbulent eddy tendencies in the azimuthally and time-averaged budget for vertical velocity [(3)]. Overall, the mean advective tendencies in the $\langle w \rangle$ budget make small contributions. The vertical turbulent tendency in Fig. A3 (third row, right) makes the largest turbulent contribution to the mean budget equation, opposing the sum of the buoyancy contribution and the vertical gradient of the normalized pressure term (third row, left).

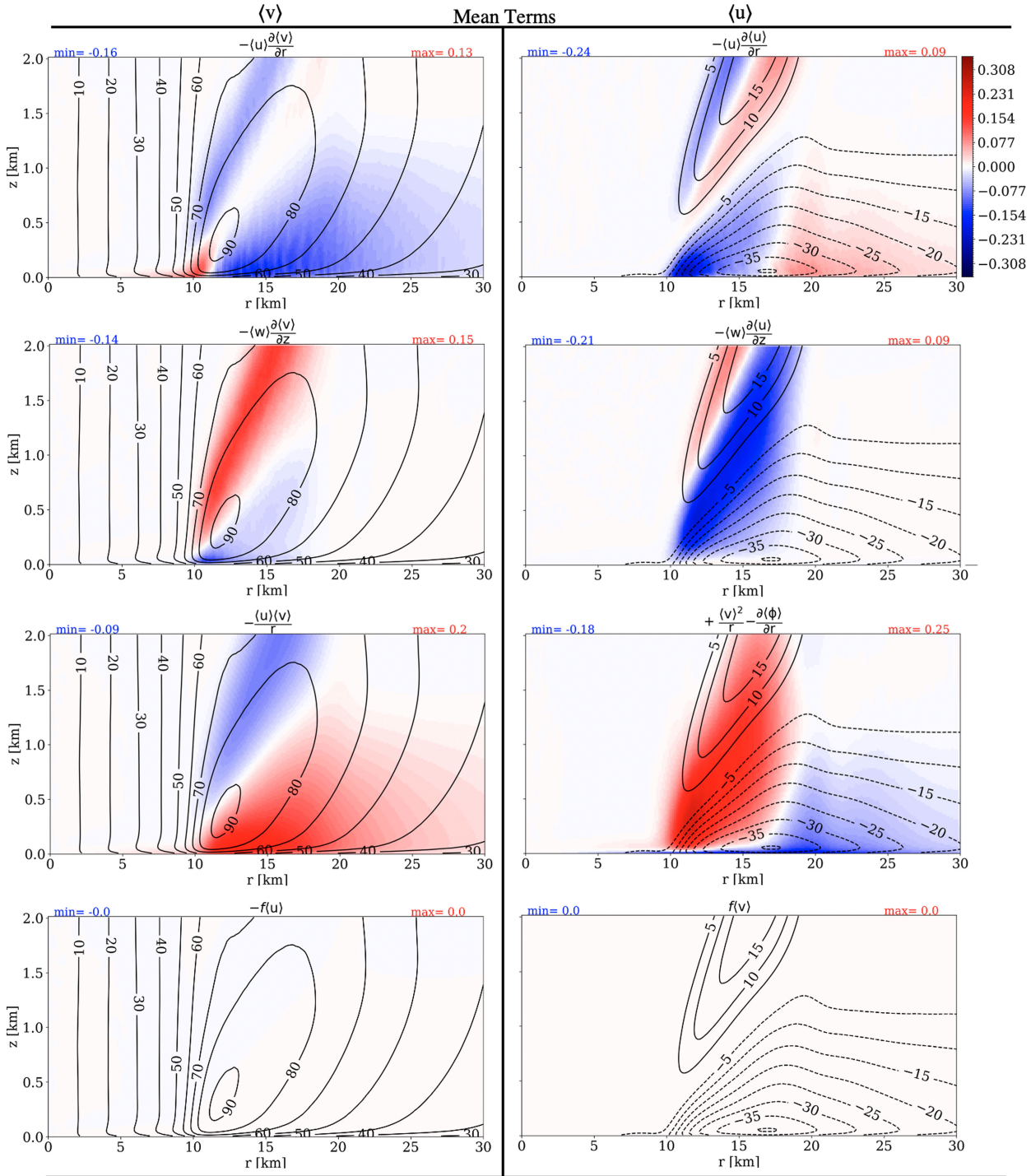


FIG. A1. As in Fig. 5, but showing the contribution from other mean-field terms in the budget equation shown in (1) and (2), as indicated at the top of each panel.

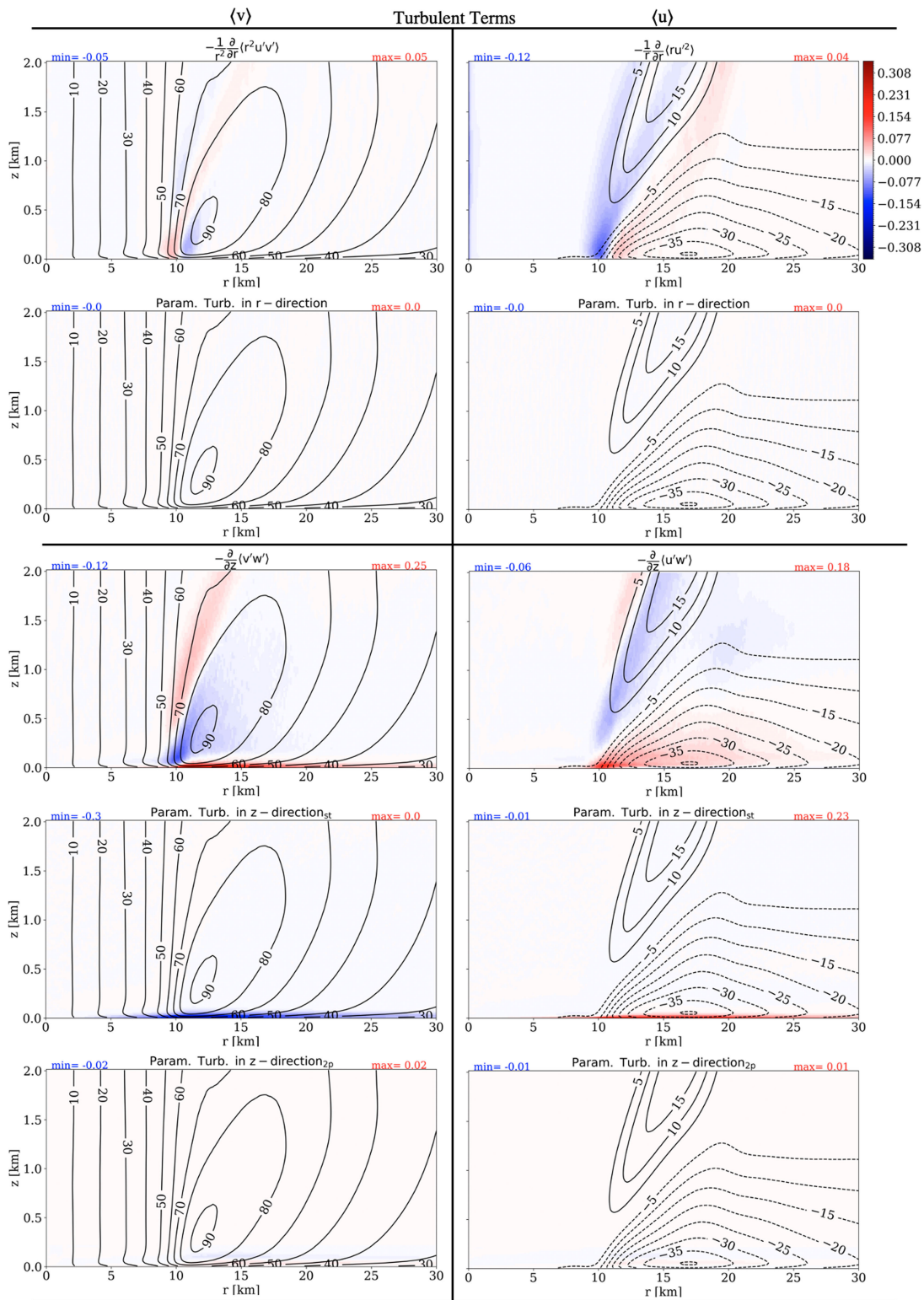


FIG. A2. As in Fig. 5, but showing terms related to the contribution of resolved and parameterized turbulence to the mean-field budget, as indicated at the top of each panel.

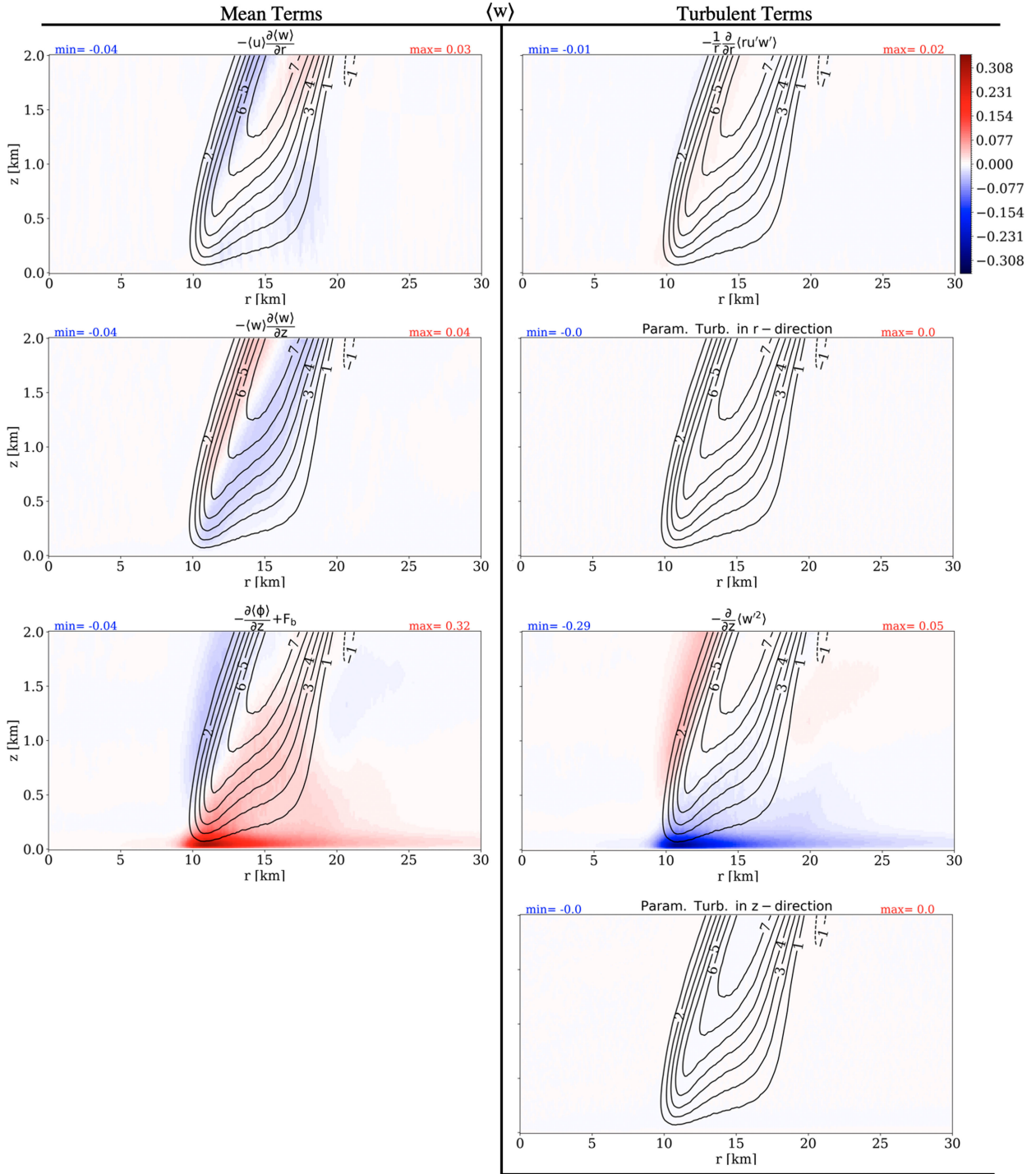


FIG. A3. As in Figs. 5e and 5f, but showing the contribution from other mean-field and turbulent terms in the budget equation shown in (3), as indicated at the top of each panel.

REFERENCES

- Aberson, S. D., M. L. Black, R. A. Black, R. W. Burpee, J. J. Cione, C. W. Landsea, and F. D. Marks Jr., 2006a: Thirty years of tropical cyclone research with the NOAA P-3 aircraft. *Bull. Amer. Meteor. Soc.*, **87**, 1039–1056, <https://doi.org/10.1175/BAMS-87-8-1039>.
- , M. T. Montgomery, M. Bell, and M. Black, 2006b: Hurricane Isabel (2003): New insights into the physics of intense storms. Part II: Extreme localized wind. *Bull. Amer. Meteor. Soc.*, **87**, 1349–1354, <https://doi.org/10.1175/BAMS-87-10-1349>.
- , J. A. Zhang, and K. N. Ocasio, 2017: An extreme event in the eyewall of Hurricane Felix on 2 September 2007. *Mon. Wea. Rev.*, **145**, 2083–2092, <https://doi.org/10.1175/MWR-D-16-0364.1>.
- Ahern, K., M. A. Bourassa, R. E. Hart, J. A. Zhang, and R. F. Rogers, 2019: Observed kinematic and thermodynamic structure in the hurricane boundary layer during intensity change. *Mon. Wea. Rev.*, **147**, 2765–2785, <https://doi.org/10.1175/MWR-D-18-0380.1>.
- Aksoy, A., J. J. Cione, B. A. Dahl, and P. D. Reasor, 2022: Tropical cyclone data assimilation with Coyote uncrewed aircraft system observations, very frequent cycling, and a new online quality control technique. *Mon. Wea. Rev.*, **150**, 797–820, <https://doi.org/10.1175/MWR-D-21-0124.1>.
- Alford, A. A., M. I. Biggerstaff, and G. Carrie, 2023: Using ground-based radar observations to evaluate asymmetric convection and eyewall dynamics during the landfall of Hurricane Harvey (2017). *J. Atmos. Sci.*, **80**, 1867–1889, <https://doi.org/10.1175/JAS-D-22-0053.1>.
- Anthes, R. A., 1974: The dynamics and energetics of mature tropical cyclones. *Rev. Geophys.*, **12**, 495–522, <https://doi.org/10.1029/RG012i003p00495>.
- Biswas, G., and V. Eswaran, 2002: *Turbulent Flows: Fundamentals, Experiments and Modeling*. CRC Press, 456 pp.
- Black, P. G., and Coauthors, 2007: Air-sea exchange in hurricanes: Synthesis of observations from the coupled boundary layer air-sea transfer experiment. *Bull. Amer. Meteor. Soc.*, **88**, 357–374, <https://doi.org/10.1175/BAMS-88-3-357>.
- Blackadar, A. K., 1962: The vertical distribution of wind and turbulent exchange in a neutral atmosphere. *J. Geophys. Res.*, **67**, 3095–3102, <https://doi.org/10.1029/JZ067i008p03095>.
- Bryan, G. H., 2012: Effects of surface exchange coefficients and turbulence length scales on the intensity and structure of numerically simulated hurricanes. *Mon. Wea. Rev.*, **140**, 1125–1143, <https://doi.org/10.1175/MWR-D-11-00231.1>.
- , and J. M. Fritsch, 2002: A benchmark simulation for moist nonhydrostatic numerical models. *Mon. Wea. Rev.*, **130**, 2917–2928, [https://doi.org/10.1175/1520-0493\(2002\)130<2917:ABSMN>2.0.CO;2](https://doi.org/10.1175/1520-0493(2002)130<2917:ABSMN>2.0.CO;2).
- , and R. Rotunno, 2009: The maximum intensity of tropical cyclones in axisymmetric numerical model simulations. *Mon. Wea. Rev.*, **137**, 1770–1789, <https://doi.org/10.1175/2008MWR2709.1>.
- , N. A. Dahl, D. S. Nolan, and R. Rotunno, 2017a: An eddy injection method for large-eddy simulations of tornado-like vortices. *Mon. Wea. Rev.*, **145**, 1937–1961, <https://doi.org/10.1175/MWR-D-16-0339.1>.
- , R. P. Worsnop, J. K. Lundquist, and J. A. Zhang, 2017b: A simple method for simulating wind profiles in the boundary layer of tropical cyclones. *Bound.-Layer Meteor.*, **162**, 475–502, <https://doi.org/10.1007/s10546-016-0207-0>.
- Byrne, D., and J. A. Zhang, 2013: Height-dependent transition from 3-D to 2-D turbulence in the hurricane boundary layer. *Geophys. Res. Lett.*, **40**, 1439–1442, <https://doi.org/10.1002/grl.50335>.
- Cangialosi, J. P., E. Blake, M. DeMaria, A. Penny, A. Latto, E. Rappaport, and V. Tallapragada, 2020: Recent progress in tropical cyclone intensity forecasting at the National Hurricane Center. *Wea. Forecasting*, **35**, 1913–1922, <https://doi.org/10.1175/WAF-D-20-0059.1>.
- Cécé, R., and Coauthors, 2021: A 30 m scale modeling of extreme gusts during Hurricane Irma (2017) landfall on very small mountainous islands in the Lesser Antilles. *Nat. Hazards Earth Syst. Sci.*, **21**, 129–145, <https://doi.org/10.5194/nhess-21-129-2021>.
- Chen, X., 2022: How do planetary boundary layer schemes perform in hurricane conditions: A comparison with large-eddy simulations. *J. Adv. Model. Earth Syst.*, **14**, e2022MS003088, <https://doi.org/10.1029/2022MS003088>.
- , and F. D. Marks, 2024: Parameterizations of boundary layer mass fluxes in high-wind conditions for tropical cyclone simulations. *J. Atmos. Sci.*, **81**, 77–91, <https://doi.org/10.1175/JAS-D-23-0086.1>.
- , G. H. Bryan, J. A. Zhang, J. J. Cione, and F. D. Marks, 2021: A framework for simulating the tropical cyclone boundary layer using large-eddy simulation and its use in evaluating PBL parameterizations. *J. Atmos. Sci.*, **78**, 3559–3574, <https://doi.org/10.1175/JAS-D-20-0227.1>.
- Cione, J. J., E. Kalina, E. Uhlhorn, A. Farber, and B. Damiano, 2016: Coyote unmanned aircraft system observations in Hurricane Edouard (2014). *Earth Space Sci.*, **3**, 370–380, <https://doi.org/10.1002/2016EA000187>.
- , and Coauthors, 2020: Eye of the storm: Observing hurricanes with a small unmanned aircraft system. *Bull. Amer. Meteor. Soc.*, **101**, E186–E205, <https://doi.org/10.1175/BAMS-D-19-0169.1>.
- Darko, J., L. Folsom, H. Park, M. Minamide, M. Ono, and H. Su, 2022: A sampling-based path planning algorithm for improving observations in tropical cyclones. *Earth Space Sci.*, **9**, e2020EA001498, <https://doi.org/10.1029/2020EA001498>.
- Deardorff, J. W., 1980: Stratocumulus-capped mixed layers derived from a three-dimensional model. *Bound.-Layer Meteor.*, **18**, 495–527, <https://doi.org/10.1007/BF00119502>.
- DeMaria, M., C. R. Sampson, J. A. Knaff, and K. D. Musgrave, 2014: Is tropical cyclone intensity guidance improving? *Bull. Amer. Meteor. Soc.*, **95**, 387–398, <https://doi.org/10.1175/BAMS-D-12-00240.1>.
- Drennan, W. M., J. A. Zhang, J. R. French, C. McCormick, and P. G. Black, 2007: Turbulent fluxes in the hurricane boundary layer. Part II: Latent heat flux. *J. Atmos. Sci.*, **64**, 1103–1115, <https://doi.org/10.1175/JAS3889.1>.
- Eliassen, A., 1959: On the formation of fronts in the atmosphere. *The Atmosphere and the Sea in Motion (Rossby Memorial Volume)*, B. Bolin, Ed., Rockefeller Institute Press, 277–287.
- Emanuel, K., 2017: Will global warming make hurricane forecasting more difficult? *Bull. Amer. Meteor. Soc.*, **98**, 495–501, <https://doi.org/10.1175/BAMS-D-16-0134.1>.
- Emanuel, K. A., 1986: An air-sea interaction theory for tropical cyclones. Part I: Steady-state maintenance. *J. Atmos. Sci.*, **43**, 585–605, [https://doi.org/10.1175/1520-0469\(1986\)043<0585:AASITF>2.0.CO;2](https://doi.org/10.1175/1520-0469(1986)043<0585:AASITF>2.0.CO;2).
- , 1997: Some aspects of hurricane inner-core dynamics and energetics. *J. Atmos. Sci.*, **54**, 1014–1026, [https://doi.org/10.1175/1520-0469\(1997\)054<1014:SAOHC>2.0.CO;2](https://doi.org/10.1175/1520-0469(1997)054<1014:SAOHC>2.0.CO;2).

- Foster, R., 2013: Signature of large aspect ratio roll vortices in synthetic aperture radar images of tropical cyclones. *Oceanography*, **26** (2), 58–67, <https://doi.org/10.5670/oceanog.2013.31>.
- Foster, R. C., 2005: Why rolls are prevalent in the hurricane boundary layer. *J. Atmos. Sci.*, **62**, 2647–2661, <https://doi.org/10.1175/JAS3475.1>.
- French, J. R., W. M. Drennan, J. A. Zhang, and P. G. Black, 2007: Turbulent fluxes in the hurricane boundary layer. Part I: Momentum flux. *J. Atmos. Sci.*, **64**, 1089–1102, <https://doi.org/10.1175/JAS3887.1>.
- Gray, W. M., 1966: On the scales of motion and internal stress characteristics of the hurricane. *J. Atmos. Sci.*, **23**, 278–288, [https://doi.org/10.1175/1520-0469\(1966\)023<0278:OTSOMA>2.0.CO;2](https://doi.org/10.1175/1520-0469(1966)023<0278:OTSOMA>2.0.CO;2).
- Guimond, S. R., G. M. Heymsfield, P. D. Reasor, and A. C. Didlake Jr., 2016: The rapid intensification of Hurricane Karl (2010): New remote sensing observations of convective bursts from the Global Hawk platform. *J. Atmos. Sci.*, **73**, 3617–3639, <https://doi.org/10.1175/JAS-D-16-0026.1>.
- , J. A. Zhang, J. W. Sapp, and S. J. Frasier, 2018: Coherent turbulence in the boundary layer of Hurricane Rita (2005) during an eyewall replacement cycle. *J. Atmos. Sci.*, **75**, 3071–3093, <https://doi.org/10.1175/JAS-D-17-0347.1>.
- Han, J., and C. S. Bretherton, 2019: TKE-based moist eddy-diffusivity mass-flux (EDMF) parameterization for vertical turbulent mixing. *Wea. Forecasting*, **34**, 869–886, <https://doi.org/10.1175/WAF-D-18-0146.1>.
- Hinze, J. O., 1959: *Turbulence*. McGraw-Hill, 568 pp.
- , 1976: Memory effects in turbulence. *Z. Angew. Math. Mech.*, **56**, T403–T415, <https://doi.org/10.1002/zamm.19760561007>.
- Holland, G. J., 1997: The maximum potential intensity of tropical cyclones. *J. Atmos. Sci.*, **54**, 2519–2541, [https://doi.org/10.1175/1520-0469\(1997\)054<2519:TMPIOT>2.0.CO;2](https://doi.org/10.1175/1520-0469(1997)054<2519:TMPIOT>2.0.CO;2).
- Ito, J., T. Oizumi, and H. Niino, 2017: Near-surface coherent structures explored by large eddy simulation of entire tropical cyclones. *Sci. Rep.*, **7**, 3798, <https://doi.org/10.1038/s41598-017-03848-w>.
- Kepert, J., and Y. Wang, 2001: The dynamics of boundary layer jets within the tropical cyclone core. Part II: Nonlinear enhancement. *J. Atmos. Sci.*, **58**, 2485–2501, [https://doi.org/10.1175/1520-0469\(2001\)058<2485:TDOBLJ>2.0.CO;2](https://doi.org/10.1175/1520-0469(2001)058<2485:TDOBLJ>2.0.CO;2).
- Kepert, J. D., 2012: Choosing a boundary layer parameterization for tropical cyclone modeling. *Mon. Wea. Rev.*, **140**, 1427–1445, <https://doi.org/10.1175/MWR-D-11-00217.1>.
- Kosiba, K. A., and J. Wurman, 2014: Finescale dual-Doppler analysis of hurricane boundary layer structures in Hurricane Frances (2004) at landfall. *Mon. Wea. Rev.*, **142**, 1874–1891, <https://doi.org/10.1175/MWR-D-13-00178.1>.
- Kossin, J. P., and W. H. Schubert, 2004: Mesovortices in hurricane Isabel. *Bull. Amer. Meteor. Soc.*, **85**, 151–153, <https://doi.org/10.1175/BAMS-85-2-151>.
- Li, X., and Z. Pu, 2023: Dynamic mechanisms associated with the structure and evolution of roll vortices and coherent turbulence in the Hurricane Boundary Layer: A large eddy simulation during the landfall of hurricane Harvey. *Bound.-Layer Meteor.*, **186**, 615–636, <https://doi.org/10.1007/s10546-022-00775-w>.
- Liu, Q., L. Wu, N. Qin, J. Song, and N. Wei, 2022: Wind gusts associated with tornado-scale vortices in the tropical cyclone boundary layer: A numerical simulation. *Front. Earth Sci.*, **10**, 945058, <https://doi.org/10.3389/feart.2022.945058>.
- Lorsolo, S., J. L. Schroeder, P. Dodge, and F. Marks Jr., 2008: An observational study of hurricane boundary layer small-scale coherent structures. *Mon. Wea. Rev.*, **136**, 2871–2893, <https://doi.org/10.1175/2008MWR2273.1>.
- , J. A. Zhang, F. Marks, and J. Gamache, 2010: Estimation and mapping of hurricane turbulent energy using airborne Doppler measurements. *Mon. Wea. Rev.*, **138**, 3656–3670, <https://doi.org/10.1175/2010MWR3183.1>.
- Louis, J.-F., 1979: A parametric model of vertical eddy fluxes in the atmosphere. *Bound.-Layer Meteor.*, **17**, 187–202, <https://doi.org/10.1007/BF00117978>.
- , M. Tiedtke, and J.-F. Geleyn, 1982: A short history of the operational PBL parameterization at ECMWF. *Workshop on Planetary Boundary Layer Parameterization*, Reading, United Kingdom, ECMWF, 59–79, <https://www.ecmwf.int/en/elibrary/75473-short-history-pbl-parameterization-ecmwf>.
- Malkus, J. S., and H. Riehl, 1960: On the dynamics and energy transformations in steady-state hurricanes. *Tellus*, **12A** (1), 1–20, <https://doi.org/10.3402/tellusa.v12i1.9351>.
- Marks, F. D., Jr., and R. A. Houze, 1987: Inner core structure of Hurricane Alicia from airborne Doppler radar observations. *J. Atmos. Sci.*, **44**, 1296–1317, [https://doi.org/10.1175/1520-0469\(1987\)044<1296:ICSOHA>2.0.CO;2](https://doi.org/10.1175/1520-0469(1987)044<1296:ICSOHA>2.0.CO;2).
- Marks, F. D., P. G. Black, M. T. Montgomery, and R. W. Burpee, 2008: Structure of the eye and eyewall of Hurricane Hugo (1989). *Mon. Wea. Rev.*, **136**, 1237–1259, <https://doi.org/10.1175/2007MWR2073.1>.
- Mason, P. J., and R. I. Sykes, 1982: A two-dimensional numerical study of horizontal roll vortices in an inversion capped planetary boundary layer. *Quart. J. Roy. Meteor. Soc.*, **108**, 801–823, <https://doi.org/10.1002/qj.49710845805>.
- , and D. J. Thomson, 1992: Stochastic backscatter in large-eddy simulations of boundary layers. *J. Fluid Mech.*, **242**, 51–78, <https://doi.org/10.1017/S0022112092002271>.
- Masters, J. M., 1999: Hunting Hugo: Ten years ago, the hurricane hunters had one of their wildest rides ever. *Weatherwise*, **52**, 20–27, <https://doi.org/10.1080/00431679909604327>.
- Ming, J., J. A. Zhang, and R. F. Rogers, 2015: Typhoon kinematic and thermodynamic boundary layer structure from dropsonde composites. *J. Geophys. Res. Atmos.*, **120**, 3158–3172, <https://doi.org/10.1002/2014JD022640>.
- Moeng, C.-H., and P. P. Sullivan, 2014: Large-eddy simulation. *Encyclopedia of Atmospheric Sciences*, 2nd ed. G. North, F. Zhang and J. Pyle, Eds., Academic Press, 232–240.
- Montgomery, M. T., and R. K. Smith, 2014: Paradigms for tropical cyclone intensification. *Aust. Meteor. Oceanogr. J.*, **64**, 37–66, <https://doi.org/10.22499/2.6401.005>.
- , and —, 2017: Recent developments in the fluid dynamics of tropical cyclones. *Annu. Rev. Fluid Mech.*, **49**, 541–574, <https://doi.org/10.1146/annurev-fluid-010816-060022>.
- , M. M. Bell, S. D. Aberson, and M. L. Black, 2006: Hurricane Isabel (2003): New insights into the physics of intense storms. Part I: Mean vortex structure and maximum intensity estimates. *Bull. Amer. Meteor. Soc.*, **87**, 1335–1348, <https://doi.org/10.1175/BAMS-87-10-1335>.
- Morrison, H., G. Thompson, and V. Tatarki, 2009: Impact of cloud microphysics on the development of trailing stratiform precipitation in a simulated squall line: Comparison of one- and two-moment schemes. *Mon. Wea. Rev.*, **137**, 991–1007, <https://doi.org/10.1175/2008MWR2556.1>.
- Morrison, I., S. Businger, F. Marks, P. Dodge, and J. A. Businger, 2005: An observational case for the prevalence of roll vortices in the hurricane boundary layer. *J. Atmos. Sci.*, **62**, 2662–2673, <https://doi.org/10.1175/JAS3508.1>.

- Muñoz-Esparza, D., B. Kosović, J. Mirocha, and J. van Beeck, 2014: Bridging the transition from mesoscale to microscale turbulence in numerical weather prediction models. *Bound.-Layer Meteor.*, **153**, 409–440, <https://doi.org/10.1007/s10546-014-9956-9>.
- Munters, W., C. Meneveau, and J. Meyers, 2016: Turbulent inflow precursor method with time-varying direction for large-eddy simulations and applications to wind farms. *Bound.-Layer Meteor.*, **159**, 305–328, <https://doi.org/10.1007/s10546-016-0127-z>.
- Nardi, K. M., C. M. Zarzycki, V. E. Larson, and G. H. Bryan, 2022: Assessing the sensitivity of the tropical cyclone boundary layer to the parameterization of momentum flux in the community earth system model. *Mon. Wea. Rev.*, **150**, 883–906, <https://doi.org/10.1175/MWR-D-21-0186.1>.
- Nolan, D. S., N. A. Dahl, G. H. Bryan, and R. Rotunno, 2017: Tornado vortex structure, intensity, and surface wind gusts in large-eddy simulations with fully developed turbulence. *J. Atmos. Sci.*, **74**, 1573–1597, <https://doi.org/10.1175/JAS-D-16-0258.1>.
- Palmén, E. H., and C. W. Newton, 1969: *Atmospheric Circulation Systems: Their Structure and Physical Interpretation*. Academic Press, 603 pp.
- Panofsky, H. A., 1953: The variation of the turbulence spectrum with height under superadiabatic conditions. *Quart. J. Roy. Meteor. Soc.*, **79**, 150–153, <https://doi.org/10.1002/qj.49707933913>.
- , and R. A. McCormick, 1960: The spectrum of vertical velocity near the surface. *Quart. J. Roy. Meteor. Soc.*, **86**, 495–503, <https://doi.org/10.1002/qj.49708637006>.
- Persing, J., M. T. Montgomery, J. C. McWilliams, and R. K. Smith, 2013: Asymmetric and axisymmetric dynamics of tropical cyclones. *Atmos. Chem. Phys.*, **13**, 12299–12341, <https://doi.org/10.5194/acp-13-12299-2013>.
- Prandtl, L., 1932: Zur turbulenten Strömung in Rohren und längs Platten. *Ergebnisse der aerodynamischen Versuchsanstalt zu Göttingen Lfg. 4*, De Gruyter, 18–29.
- Protzko, D. E., S. R. Guimond, C. R. Jackson, J. W. Sapp, Z. Jelenak, and P. S. Chang, 2023: Documenting coherent turbulent structures in the boundary layer of intense hurricanes through Wavelet Analysis on IWRAP and SAR data. *IEEE Trans. Geosci. Remote Sens.*, **61**, 4105316, <https://doi.org/10.1109/TGRS.2023.3305998>.
- Richter, D. H., C. Wainwright, D. P. Stern, G. H. Bryan, and D. Chavas, 2021: Potential low bias in high-wind drag coefficient inferred from dropsonde data in hurricanes. *J. Atmos. Sci.*, **78**, 2339–2352, <https://doi.org/10.1175/JAS-D-20-0390.1>.
- Rogers, R., and Coauthors, 2006: The Intensity Forecasting Experiment: A NOAA multiyear field program for improving tropical cyclone intensity forecasts. *Bull. Amer. Meteor. Soc.*, **87**, 1523–1538, <https://doi.org/10.1175/BAMS-87-11-1523>.
- , S. Lorsolo, P. Reasor, J. Gamache, and F. Marks, 2012: Multiscale analysis of tropical cyclone kinematic structure from airborne Doppler radar composites. *Mon. Wea. Rev.*, **140**, 77–99, <https://doi.org/10.1175/MWR-D-10-05075.1>.
- Rossby, C., and R. B. Montgomery, 1935: *The Layer of Frictional Influence in Wind and Ocean Currents. Papers in Physical Oceanography and Meteorology*. Vol. 3. Massachusetts Institute of Technology and Woods Hole Oceanographic Institution, 101 pp.
- Rotunno, R., and K. A. Emanuel, 1987: An air-sea interaction theory for tropical cyclones. Part II: Evolutionary study using a nonhydrostatic axisymmetric numerical model. *J. Atmos. Sci.*, **44**, 542–561, [https://doi.org/10.1175/1520-0469\(1987\)044<0542:AAITFT>2.0.CO;2](https://doi.org/10.1175/1520-0469(1987)044<0542:AAITFT>2.0.CO;2).
- , and G. H. Bryan, 2012: Effects of parameterized diffusion on simulated hurricanes. *J. Atmos. Sci.*, **69**, 2284–2299, <https://doi.org/10.1175/JAS-D-11-0204.1>.
- , Y. Chen, W. Wang, C. Davis, J. Dudhia, and G. Holland, 2009: Large-eddy simulation of an idealized tropical cyclone. *Bull. Amer. Meteor. Soc.*, **90**, 1783–1788, <https://doi.org/10.1175/2009BAMS2884.1>.
- Rozoff, C. M., D. S. Nolan, G. H. Bryan, E. A. Hendricks, and J. Knilev, 2023: Large-eddy simulations of the tropical cyclone boundary layer at landfall in an idealized urban environment. *J. Appl. Meteor. Climatol.*, **62**, 1457–1478, <https://doi.org/10.1175/JAMC-D-23-0024.1>.
- Schlichting, H., and J. Kestin, 1961: *Boundary Layer Theory*. Vol. 121, Springer, 817 pp.
- Sellwood, K. J., J. A. Sippel, and A. Aksoy, 2023: Assimilation of coyote small uncrewed aircraft system observations in Hurricane Maria (2017) using operational HWRF. *Wea. Forecasting*, **38**, 901–919, <https://doi.org/10.1175/WAF-D-22-0214.1>.
- Shea, D. J., and W. M. Gray, 1973: The hurricane's inner core region. I. Symmetric and asymmetric structure. *J. Atmos. Sci.*, **30**, 1544–1564, [https://doi.org/10.1175/1520-0469\(1973\)030<1544:THICRI>2.0.CO;2](https://doi.org/10.1175/1520-0469(1973)030<1544:THICRI>2.0.CO;2).
- Smagorinsky, J., 1963: General circulation experiments with the primitive equations: I. The basic experiment. *Mon. Wea. Rev.*, **91**, 99–164, [https://doi.org/10.1175/1520-0493\(1963\)091<099:GCEWTP>2.3.CO;2](https://doi.org/10.1175/1520-0493(1963)091<099:GCEWTP>2.3.CO;2).
- Smith, R. K., and M. T. Montgomery, 2010: Hurricane boundary-layer theory. *Quart. J. Roy. Meteor. Soc.*, **136**, 1665–1670, <https://doi.org/10.1002/qj.679>.
- , —, and N. Van Sang, 2009: Tropical cyclone spin-up revisited. *Quart. J. Roy. Meteor. Soc.*, **135**, 1321–1335, <https://doi.org/10.1002/qj.428>.
- Sparks, N., K. K. Hon, P. W. Chan, S. Wang, J. C. L. Chan, T. C. Lee, and R. Toumi, 2019: Aircraft observations of tropical cyclone boundary layer turbulence over the South China Sea. *J. Atmos. Sci.*, **76**, 3773–3783, <https://doi.org/10.1175/JAS-D-19-0128.1>.
- Stanisic, M. M., 2012: *The Mathematical Theory of Turbulence*. Springer Science and Business Media, 429 pp.
- Stern, D. P., and G. H. Bryan, 2018: Using simulated dropsondes to understand extreme updrafts and wind speeds in tropical cyclones. *Mon. Wea. Rev.*, **146**, 3901–3925, <https://doi.org/10.1175/MWR-D-18-0041.1>.
- , —, and S. D. Aberson, 2016: Extreme low-level updrafts and wind speeds measured by dropsondes in tropical cyclones. *Mon. Wea. Rev.*, **144**, 2177–2204, <https://doi.org/10.1175/MWR-D-15-0313.1>.
- , —, C.-Y. Lee, and J. D. Doyle, 2021: Estimating the risk of extreme wind gusts in tropical cyclones using idealized large-eddy simulations and a statistical-dynamical model. *Mon. Wea. Rev.*, **149**, 4183–4204, <https://doi.org/10.1175/MWR-D-21-0059.1>.
- Stull, R. B., 1988: *An Introduction to Boundary Layer Meteorology*. Vol. 13, Springer Science and Business Media, 670 pp.
- Sullivan, P. P., J. C. McWilliams, J. C. Weil, E. G. Patton, and H. J. S. Fernando, 2020: Marine atmospheric boundary layers above heterogeneous SST: Across-front winds. *J. Atmos. Sci.*, **77**, 4251–4275, <https://doi.org/10.1175/JAS-D-20-0062.1>.
- Tang, J., D. Byrne, J. A. Zhang, Y. Wang, X.-t. Lei, D. Wu, P.-z. Fang, and B.-k. Zhao, 2015: Horizontal transition of turbulent cascade in the near-surface layer of tropical cyclones. *J. Atmos. Sci.*, **72**, 4915–4925, <https://doi.org/10.1175/JAS-D-14-0373.1>.

- Tennekes, H., and J. L. Lumley, 1972: *A First Course in Turbulence*. MIT Press, 320 pp.
- Tsukada, T., and T. Horinouchi, 2020: Estimation of the tangential winds and asymmetric structures in typhoon inner core region using Himawari-8. *Geophys. Res. Lett.*, **47**, e2020GL087637, <https://doi.org/10.1029/2020GL087637>.
- Wajsowicz, R. C., 1993: A consistent formulation of the anisotropic stress tensor for use in models of the large-scale ocean circulation. *J. Comput. Phys.*, **105**, 333–338, <https://doi.org/10.1006/jcph.1993.1079>.
- Wang, A., Y. Pan, G. H. Bryan, and P. M. Markowski, 2023: Modeling near-surface turbulence in large-eddy simulations of a tornado: An application of thin boundary layer equations. *Mon. Wea. Rev.*, **151**, 1587–1607, <https://doi.org/10.1175/MWR-D-22-0060.1>.
- Wang, S., and Q. Jiang, 2017: Impact of vertical wind shear on roll structure in idealized hurricane boundary layers. *Atmos. Chem. Phys.*, **17**, 3507–3524, <https://doi.org/10.5194/acp-17-3507-2017>.
- Wicker, L. J., and W. C. Skamarock, 2002: Time-splitting methods for elastic models using forward time schemes. *Mon. Wea. Rev.*, **130**, 2088–2097, [https://doi.org/10.1175/1520-0493\(2002\)130<2088:TSMFEM>2.0.CO;2](https://doi.org/10.1175/1520-0493(2002)130<2088:TSMFEM>2.0.CO;2).
- Worsnop, R. P., G. H. Bryan, J. K. Lundquist, and J. A. Zhang, 2017: Using large-eddy simulations to define spectral and coherence characteristics of the hurricane boundary layer for wind-energy applications. *Bound.-Layer Meteor.*, **165**, 55–86, <https://doi.org/10.1007/s10546-017-0266-x>.
- Wu, L., Q. Liu, and Y. Li, 2018: Prevalence of tornado-scale vortices in the tropical cyclone eyewall. *Proc. Natl. Acad. Sci. USA*, **115**, 8307–8310, <https://doi.org/10.1073/pnas.1807217115>.
- , —, and —, 2019: Tornado-scale vortices in the tropical cyclone boundary layer: Numerical simulation with the WRF-LES framework. *Atmos. Chem. Phys.*, **19**, 2477–2487, <https://doi.org/10.5194/acp-19-2477-2019>.
- Wurman, J., and J. Winslow, 1998: Intense sub-kilometer-scale boundary layer rolls observed in Hurricane Fran. *Science*, **280**, 555–557, <https://doi.org/10.1126/science.280.5363.555>.
- , —, and K. Kosiba, 2018: The role of small-scale vortices in enhancing surface winds and damage in Hurricane Harvey (2017). *Mon. Wea. Rev.*, **146**, 713–722, <https://doi.org/10.1175/MWR-D-17-0327.1>.
- Zhang, J. A., and W. M. Drennan, 2012: An observational study of vertical eddy diffusivity in the hurricane boundary layer. *J. Atmos. Sci.*, **69**, 3223–3236, <https://doi.org/10.1175/JAS-D-11-0348.1>.
- , and M. T. Montgomery, 2012: Observational estimates of the horizontal eddy diffusivity and mixing length in the low-level region of intense hurricanes. *J. Atmos. Sci.*, **69**, 1306–1316, <https://doi.org/10.1175/JAS-D-11-0180.1>.
- , and F. D. Marks, 2015: Effects of horizontal diffusion on tropical cyclone intensity change and structure in idealized three-dimensional numerical simulations. *Mon. Wea. Rev.*, **143**, 3981–3995, <https://doi.org/10.1175/MWR-D-14-00341.1>.
- , W. M. Drennan, P. G. Black, and J. R. French, 2009: Turbulence structure of the hurricane boundary layer between the outer rainbands. *J. Atmos. Sci.*, **66**, 2455–2467, <https://doi.org/10.1175/2009JAS2954.1>.
- , F. D. Marks, M. T. Montgomery, and S. Lorsolo, 2010: An estimation of turbulent characteristics in the low-level region of intense Hurricanes Allen (1980) and Hugo (1989). *Mon. Wea. Rev.*, **139**, 1447–1462, <https://doi.org/10.1175/2010MWR3435.1>.
- , R. F. Rogers, D. S. Nolan, and F. D. Marks Jr., 2011: On the characteristic height scales of the hurricane boundary layer. *Mon. Wea. Rev.*, **139**, 2523–2535, <https://doi.org/10.1175/MWR-D-10-05017.1>.
- , —, P. D. Reasor, and J. Gamache, 2023: The mean kinematic structure of the tropical cyclone boundary layer and its relationship to intensity change. *Mon. Wea. Rev.*, **151**, 63–84, <https://doi.org/10.1175/MWR-D-21-0335.1>.
- Zhu, P., 2008: Simulation and parameterization of the turbulent transport in the hurricane boundary layer by large eddies. *J. Geophys. Res.*, **113**, D17104, <https://doi.org/10.1029/2007JD009643>.